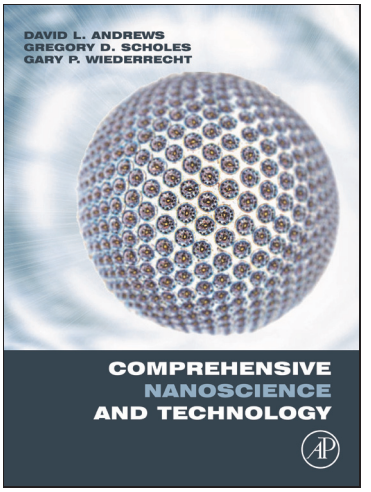

Y Chao (2011) Optical Properties of Nanostructured Silicon. In: Andrews DL, Scholes, GD and Wiederrecht GP (eds.), *Comprehensive Nanoscience and Technology*, volume 1, pp. 543–570 Oxford: Academic Press.

1.16 Optical Properties of Nanostructured Silicon

Y Chao, University of East Anglia, Norwich, UK

1.16.1 Introduction

Porous silicon (π-Si), typically a few micrometers-thick film, produced by electrochemical etching of silicon wafer in a HF solution under an anodic current, was first discovered in 1956 by Uhlir [1] at Bell's Laboratories in USA, when he was working on electrolytic shaping of the surface of silicon and germanium. However, this result did not evoke further attention from scientific communities. In 1990, Canham reported the discovery of significant visible light emission from porous silicon under the ultraviolet (UV) excitation [2]. This finding stimulated the interest of the scientific community in the material's optical and electronic properties. It is generally considered that the luminescence is owing to the presence of quantum-confined structures and the material is often described as a nanocrystalline film. Porous silicon can be broken up into individual nanoparticles by a variety of means including ultrasound [3]. It therefore provides one of the simplest routes to silicon nanoparticles, requiring only a small power supply (e.g., 400 mA, 40 V) for the etching and an ultrasonic horn or bath. In this chapter, the fabrication methods are reviewed first, followed by discussions on microstructures and quantum effect, and optical spectroscopic results and applications.

1.16.2 Fabrication Methods

The porous layer is created by electrochemical dissolution (anodization or etching) in HF-based electrolytes. It is based on the fact that holes are necessary for the electrochemical dissolution process of Si. Holes (H^+) arriving at the Si:HF solution interface etch the Si lattice as described below:

$$\mathrm{Si} + 6\mathrm{HF} \xrightarrow{\mathrm{EtOH}} \mathrm{H_2SiF_6} + \mathrm{H_2}\ \ \mathrm{np} - \mathrm{SiH} + 2\mathrm{H^+} + 2\mathrm{e^-} \tag{1}$$

Etching creates a rough surface. Since the bandgap in π-Si increases compared with bulk crystal silicon (c-Si) due to the quantum-confinement effect [4], holes need the additional energy E_q to penetrate into the porous layer. If E_q is larger than the bias, the

Comprehensive Nanoscience and Technology, 2011, Vol. 1, 543-570

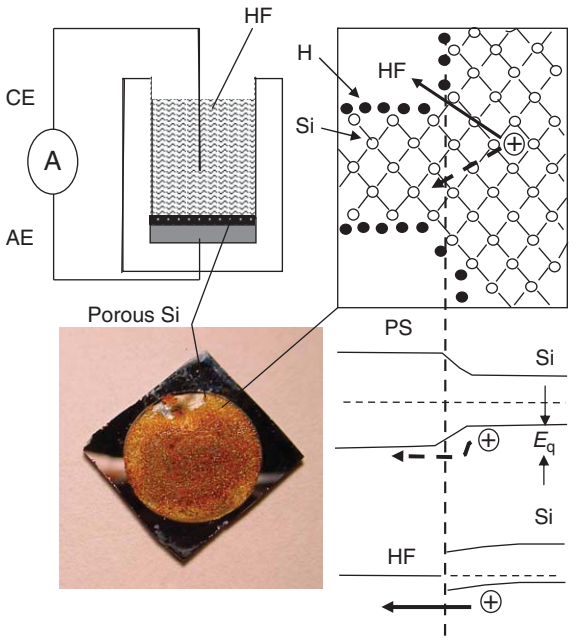

Figure 1 Schematic of porous Si fabrication, the chemical process in anodic etching near the pore tip and the band diagram for silicon–electrolyte transition at the pore tip and between the bulk and porous Si.

porous layer becomes depleted of holes and further dissolution is stopped. Since E_q is a function of the size of the nanocrystals (NCs), an increase in the formation bias will result in an increase in bandgap energy and a decrease in crystallite size in the porous layer. This process is self-adjusting. The quantum-confinement effect limits the size of the NCs [5]. **Figure 1** schematically illustrates porous Si fabrication, the chemical process in anodic etching near the pore tip and the band diagram for silicon–electrolyte transition at the pore tip and between the bulk and porous Si [4].

Another factor is that different etching current densities could affect the quality of porous silicon [6]. **Figure 2** shows the surface aspects of silicon

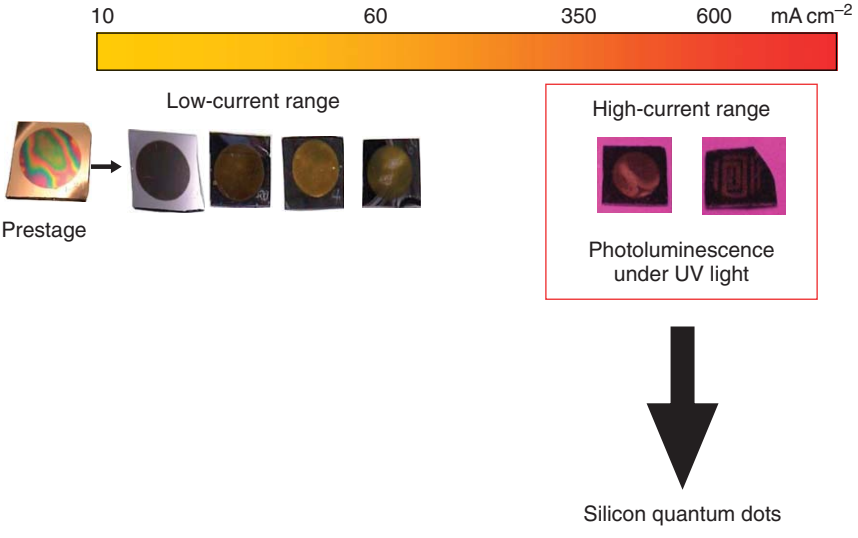

Figure 2 The surface aspects of silicon chips after electrochemical etching at different current densities, higher current density needed for preparing luminescent silicon quantum dots.

chips after electrochemical etching at different current densities. To obtain high-quality luminescent porous silicon, higher current density is required.

Silicon nanoparticles, also known as silicon quantum dots (Si-QDs), can be made by a variety of routes, which may be classified roughly as 'chemical' or 'physical'. Physical routes generally involve high temperature and/or vacuum deposition techniques and are favored when the object is to produce small quantities of material for physical or electronic applications. Chemical routes tend to produce material of less well-defined composition and size (with some exceptions), but often produce rather large amounts of material and may be compatible with the conjugation of biological molecules at the particle surface.

As there is a wealth of literature on porous silicon and reviews of its surface chemistry [7], here we mainly review preparations of samples consisting of individual silicon nanoparticles.

1.16.2.1 Electrochemical Etching and Ultrasonication

In 1990, Canham [2] was the first person to show that certain porous silicon materials can have large photoluminescence (PL) efficiency at room temperature in the visible region. He presented indirect evidence that free-standing Si quantum wires could be fabricated without the use of epitaxial deposition or lithography. His approach used electrochemical and chemical dissolution steps to define networks of isolated wires out of bulk wafers. Mesoporous Si layers of high porosity exhibited visible (red) PL at room temperature, observable with the naked eye under <1 mW unfocused green or blue laser excitation. This was attributed to dramatic two-dimensional quantum size effects which could produce emission far above the bandgap of bulk crystalline Si. Individual silicon nanoparticles with broad size distribution, but bright orange emission were produced from porous silicon by sonication a couple of years later [3].

Wolkin *et al.* [8] prepared porous Si-QD samples by electrochemical etching followed by photo-assisted stain etching of 6 Ω cm p-type Si wafers at current densities of 8–50 mA cm^{-2} using 10–25% HF:ethanol solutions. The stain etching was accomplished under illumination, with a 500 W halogen lamp and was used to further increase the porosity. Wolkin *et al.* found that depending on the size, the PL of Si-QDs present in porous silicon could be tuned from the near infrared to the ultraviolet (UV) when the surface was passivated with silicon–hydrogen (Si–H) bonds. After exposure to oxygen, the PL shifted to the red by as much as 1 eV. This shift and the changes in PL intensity and decay time showed that both quantum confinement and surface passivation affected the electronic states of Si-QDs. They found a theoretical model, in which new electronic states appear in the bandgap of the smaller QDs when a Si═O bond is formed, was in good agreement with experimental results.

Sweryda-Krawiec *et al.* [9] produced colloidal solutions of Si NCs by sonicating porous silicon wafers (suspended in 5 ml of degassed toluene) for 60–90 min in closed vials. During sonication, crystallites leached out from the porous Si network and the toluene suspension became pale yellow. Then, they modified the surface of the silicon nanocrystals (Si NCs) using alcohols. Room-temperature addition of 1-undecanol, 1-hexadecanol, 1-octanol, and 1,12-dodecanediol completely quenched the PL of Si NCs. Heating the NCs with 1-undecanol, 1-hexadecanol, and 1-octanol resulted in the partial recovery of the PL and in the formation of 1–10 nm diameter alcohol-capped Si NCs. Heating the Si NCs with 1,12-dodecanediol also partially restored the PL. Transmission electron microscope (TEM) and atomic force microscopy (AFM) images indicated the formation of diol interconnected 100–800 nm diameter silicon nanoparticle agglomerates.

Belomoin *et al.* [10] demonstrated that electrochemically etched, hydrogen-capped Si_nH_x clusters with n larger than 20 are obtained as a family of discrete sizes. These sizes are 1.0 (Si_{29}), 1.67 (Si_{123}), 2.15, 2.9, and 3.7 nm in diameter. They characterized the particles through direct electron imaging, excitation and emission optical spectroscopy, and colloidal crystallization. The bandgaps and emission bands were measured. The smallest four were ultrabright blue, green, yellow, and red luminescent particles. The blue particles were obtained by brief treatment of the wafer in an ultrasonic bath, where the film crumbled into a colloidal suspension of ultrasmall blue particles. As noted by the authors the availability of discrete sizes and distinct emission in the red, green, and blue (RGB) range is useful for biomedical tagging, RGB displays, and floating gate memories.

Lie *et al.* [6] produced Si-QDs by refluxing porous silicon in toluene solutions of alkenes. The porous layer breaks up under the conditions of the reflux and the alkene is hydrosilated at the particle surface to form a hydrocarbon monolayer which protects the

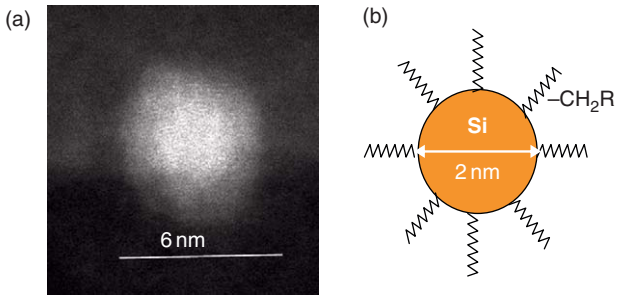

Figure 3 (a) A high-resolution transmission electron microscope (HRTEM) image of the alkylated silicon nanocrystal and (b) a schematic structure of the alkylated silicon nanocrystal.

particles and solubilizes them in organic solvents. The size of the silicon core of these particles was about 2.5 nm diameter from a combination of PL, scanning tunneling microscopy (STM), and Raman measurements. **Figure 3(a)** shows a high-resolution transmission electron microscope (HRTEM) image of an alkylated Si NC, which is a direct measurement of the nanoparticle size. **Figure 3(b)** is a schematic structure of the alkylated Si NC. The prepared alkylated Si NCs can be redispersed in organic solvents and cast as a film[11–13].

Cichos *et al.* [14] and, more recently, Valenta *et al.* [15] also prepared colloidal suspensions of Si NCs from light-emitting porous Si grains. Valenta *et al.* obtained nanoparticles by mechanical pulverization of electrochemically etched layers. Sedimented and/or filtered Si NCs sols revealed a green PL band around 530 nm, which was interpreted as radiative recombination of electron–hole pairs inside Si NCs with diameter of about 2 nm. Single-molecule spectroscopy techniques could be applied to investigate PL of single grains of Si NCs dispersed on substrates from highly diluted solutions. On the other hand, their preparation of concentrated suspensions enabled Valenta *et al.* to fabricate bulk samples with embedded Si NCs or to prepare self-organized nanostructures on surfaces. They acknowledge, however, that there are many technological aspects to improve. In particular, an efficient method to break the micrometer-sized grains of porous silicon into submicron parts has yet to be developed.

Lee *et al.* [16] produced white-light-emitting silicon nanoparticles, whose surfaces were passivated with butyl, using focused ultrasound. The white-light emission was achieved by controlling the size distribution (without the need to add any fluorescent ions). The white-light-emitting silicon nanoparticles had a wide size distribution of 1–5 nm with an average size of 2.7 nm, which were sufficiently small to indicate the quantum-confinement effect for silicon. The PL spectrum covered a wide range (320–700 nm) with a full width at half maximum of approximately 190 nm.

1.16.2.2 Other Methods

The other methods to produce porous silicon-related nanostructures include reactive sputtering [17], sol-gel techniques [18], SiO_2 implantation [19], self-assembly [20], growth in inverse micelles [21,22], laser ablation [23], thermal annealing [24–26], thermal vaporization [27,28], decomposition of silanes [29–33], solution synthesis [34–36], hybrid techniques [37], and plasma processing [38–40].

1.16.3 PL Spectroscopy

PL in visible range is a key optical feature of porous silicon. Since Canham [2] showed that nanocrystalline porous silicon can have large PL efficiency at room temperature in the visible region, porous silicon has stimulated the interests of scientific community, which is a testament not only to its technological potential but also to the fundamental interest in understanding luminescence phenomena in this material.

PL from porous silicon could be excited by laser, UV, vacuum ultraviolet (VUV), or X-ray, the light sources with the photon energy greater than the bandgap of porous silicon. **Figure 4** shows a typical PL spectrum from porous silicon excited by an argon laser at 488 nm. The PL peak wavelength is about 589 nm, which is equivalent of 2.1 eV in energy. The PL peak position is related to the bandgap of silicon

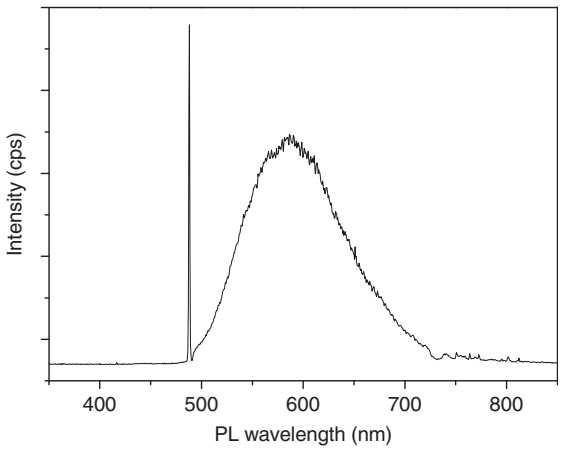

Figure 4 A typical photoluminescence spectrum from porous silicon excited by 488 nm argon laser.

nanostructures, which is affected by the structure size, defect states, and surface states.

1.16.3.1 Size Effect on the Peak Position of PL

When Si nanostructures become smaller than 20–30 nm, the transport, electronic, and optical properties of silicon start to be influenced significantly by quantum-confinement effects [41]. For example, the bandgap of bulk c-Si is 1.12 eV, but the PL peak energy of π-Si is much bigger than this value. One explanation is that the bandgap of π-Si is much bigger than that of c-Si. That means due to quantum confinement, the conduction band (CB) energy increased, while valence band (VB) energy reduced.

Figure 5 shows the CB edge shift determined from L-edge data as a function of the VB shift determined from photoemission, for a series of different samples [28]. Careful inspiration indicated that the confinement decreases the VB edge twice as much as it increases the CB edge, in agreement with effective mass theory [42]. **Figure 6** illustrates this relationship. Since the VB shift is equal to twice the CB band shift, the bandgap of π-Si samples is obtained from [28]

$$E_{\text{gap}} = \ddot{A}E_{\text{vb}} + \ddot{A}E_{\text{cb}} + 1.12\,\text{eV} = 3\ddot{A}E_{\text{cb}} + 1.12\,\text{eV} \quad (2)$$

The PL peak position of luminescent porous silicon (π-Si) should equal to the bandgap energy minus the binding energy of the excitation [43]. The difference between bandgap energy and PL energy is called Stokes shift. For example, in π-Si samples having peak PL energy of 2 eV (orange), the CB edge increased by 0.5 eV and VB edge decreased by 1 eV compared to bulk c-Si. Thus, the bandgap of these samples was 2.6 eV, while the PL was at 2 eV. **Figure 7** is a compilation of several experimental and theoretical results and shows that the Stokes shift between bandgap and PL energies increases with decreasing size.

For sizes above 3 nm, the difference between bandgap and PL energies remains below 300 meV, a value that could be attributed to exciton-binding

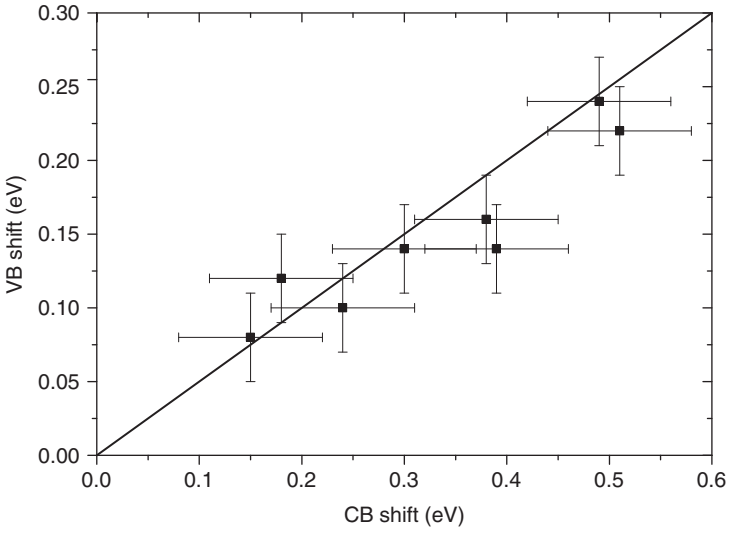

Figure 5 The conductance band (CB) shift vs. the valence band (VB) shift for a series of silicon nanoclusters. The solid line represents a 2:1 ratio between VB shift and the CB shift.

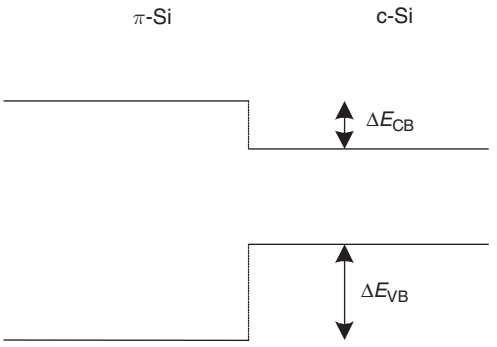

Figure 6 Increase in the conduction band energy vs. decrease in the valence band (VB) energy for π-Si samples. The effect of quantization in the VB is twice as large as in the conduction band (CB).

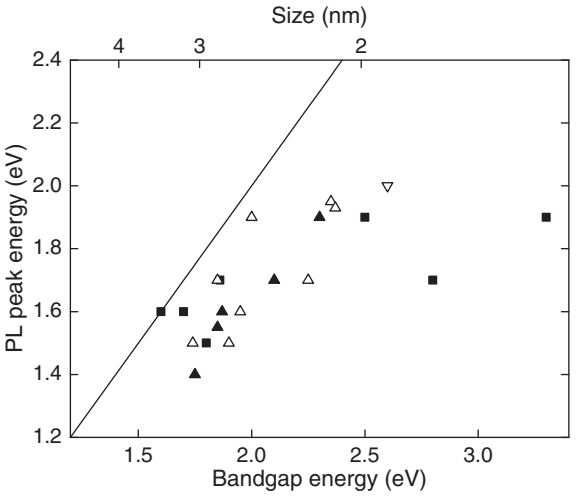

Figure 7 A compilation of several experimental and theoretical results: Photoluminescence (PL) peak energy vs. bandgap energy in π-Si. If the PL and bandgap energies were the same, the data would fall on the solid line. An early version of this plot appears in Fauchet PM (1998) Porous silicon: Photoluminescence and electroluminescent devices. In: Lockwood DJ (ed.) *Light Emission in Silicon from Physics to Devices*, p. 205. New York: Academic Press.

energy in small crystallites; however, below 3 nm, the difference appears to be too large (up to 1 eV and more) to be explained by the expected increase in the free-exciton-binding energy. It seems likely that the luminescence does not coincide with the bandgap and thus involves surface states [43].

1.16.3.2 Temperature-Dependent PL

Kapoor *et al.* [44] discussed temperature-dependent behavior of luminescence from semiconductor NCs by using the luminescence decay time τ, which can be expressed in terms of the competition between the radiative decay and nonradiative (or hopping) decay dynamics. Thus

$$\frac{1}{\tau} = R_r + R_{hop} \tag{3}$$

where R_r represents the radiative recombination rate and R_{hop} the hopping escape rate. Earlier studies [45, 46] of the radiative process posit a temperature dependence of the Arrhenius type

$$R_r = \nu_r \exp\left(-\frac{T_r}{T}\right) \tag{4}$$

where T_r is a characteristic activation temperature and ν_r a characteristic frequency. Suemoto and coworkers obtained a value of 3.5 meV for the activation energy (kT_r) based on the time dependence of PL [46]. They also obtained a value of 5000 s^{-1} for R_r. Porous silicon is a highly disordered sample-dependent system. The singlet–triplet splitting energy of the exciton is in the range of 3–10 meV. We therefore assume that the activation energy is in the range of 3–10 meV and this translates to the range of 25–135 K for the characteristic temperature T_r. This is in consistent with the 3–17 meV range reported recently by Kanemitsu [45].

There exists some evidence [44] that the hopping term has an anomalous Berthelot type of temperature dependence,

$$R_{hop} = \nu_B \exp\left(\frac{T}{T_B}\right) \tag{5}$$

where T_B is the characteristic Berthelot temperature associated with the escape process and ν_B a characteristic frequency. The varied optical behavior can be analyzed in terms of the competition between the radiative and the hopping process.

The intensity of the PL line is expressed as

$$I(t) = N(t)R_r$$

where R_r is the radiative recombination rate and $N(t)$ is the population of the excited carriers at time t,

$$N(t) = N_0 \exp\left[-\left(\frac{t}{\tau}\right)^p\right] \tag{6}$$

Here, τ is the characteristic lifetime associated with the Kohlrausch (stretched exponential) decay. Porous silicon is a disordered system and the time dependence of the PL intensity has been reported to be of the Kohlrausch type [44] with $0 < p < 1$. Thus

$$I(t,\tau) = N_0 R_r \exp\left[-\left(\frac{t}{\tau}\right)^p\right]$$

The time-integrated luminescence intensity is then given by

$$I(\tau) = \int_0^\infty I(t,\tau)\mathrm{d}t = \frac{N_0\Gamma\left(\frac{1}{p}\right)R_r\tau}{p}$$

Note that the above expression reduces to $N_0R_r\tau$ for the pure exponential case ($p=1$). Defining $I_0 = N_0$ $\tilde{A}(1/p)/p$ we have

$$I(\tau) = I_0R_r\tau \tag{7}$$

The characteristic lifetime is determined by the radiative recombination rate (R_r) and the hopping escape rate (R_{hop}).

Employing equations 3–5 in equation 7, we obtain

$$I(T) = \frac{I_0}{1+\nu_0\exp\left[\frac{T}{T_B}+\frac{T_r}{T}\right]} \tag{8}$$

where $\nu_0 = \nu_B/\nu_r$ is the reduced frequency. The temperature dependence of the PL intensity is explicitly displayed in equation 8.

The asymptotic limits of the above expression are

$$I(T)_{T\to 0} = 0 \quad \text{as} \exp[-T_r/T]$$

$$I(T)_{T\to\infty} = 0 \quad \text{as} \exp[-T/T_B]$$

It is clear from the above expressions that the PL intensity will have a maximum at some intermediate temperature T_m. This can easily be obtained to be the geometric mean of the characteristic temperatures

$$T_m = \sqrt{T_r T_B} \tag{9}$$

The possible range of the characteristic temperatures has been discussed earlier. Based on these *a priori* assignment of ranges the maxima for a PL emission line $T_m \sim 100$ K.

1.16.3.3 Origin of the Orange and Blue PL Emission

In this section, the partially oxidized Si NCs are taken as an example, and used to discus the temperature-dependent behavior of PL in order to reveal the origin of the PL emission. **Figure 8** shows PL spectra

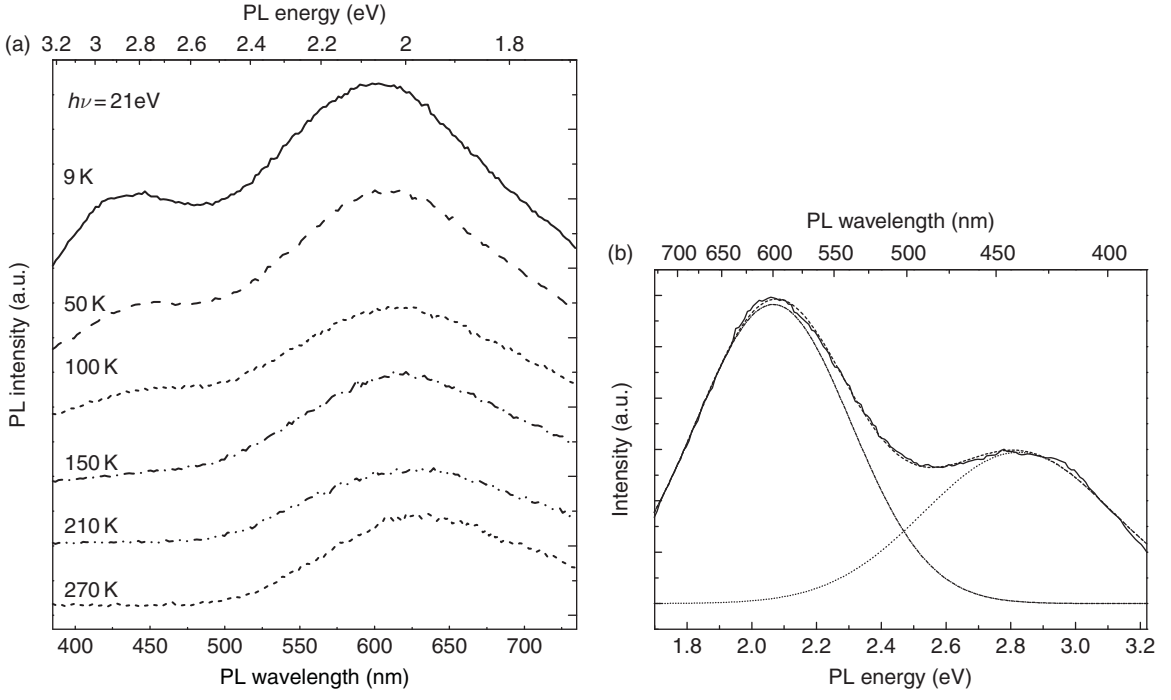

Figure 8 (a) Luminescence spectra (excitation energy = 21 eV) obtained over a temperature range of 9–270 K. As the temperature increases, the peak positions shift to higher wavelengths: the orange peak occurs at 600 nm (9 K) and 630 nm (270 K). Individual spectra are offset on the *y*-axis for clarity. (b) Gaussian fit to the 9 K data to extract the peak intensity. From Chao Y, *et al*. (2006) Optical luminescence from alkyl-passivated Si nanocrystals under vacuum ultraviolet excitation: Origin and temperature dependence of the blue and orange emissions. *Applied Physics Letters* 88(26): 263119.

from alkylated Si NCs obtained by excitation with 21 eV VUV photons at 9, 50, 100, 150, and 270 K. One can clearly see two intense visible emissions from Si NCs at temperatures lower than 150 K. The emission peak positions at 9 K were at wavelengths of 430 ± 2 nm (blue) and 600 ± 2 nm (orange), respectively. Komuro *et al.* [47] have reported two emission bands from porous silicon but their spectra did not show two such intense peaks simultaneously. Other workers have observed both blue and orange bands in time-resolved PL from porous silicon [48] and during atmospheric oxidation of uncapped Si NCs (steady-state PL) [49–51]. These studies are consistent with an interpretation that the blue emission is associated with Si oxides and that the orange PL is particle size-dependent and derives from the quantum-confinement effect in Si. Blue emission has been observed from Si and C implanted in SiO_2 matrices [52] and from carbon-plasma-implanted porous silicon, [53] but the orange emission of porous silicon disappeared after implantation. There are at least two plausible reasons for the observation of two emission bands. First, there may be a bimodal distribution of Si NC sizes, giving rise to the two observed photon energies. Second, the two PL emission bands may result from different chemical states of Si: unoxidized Si such as Si–Si bonds in the silicon core, and oxidized Si atoms such as Si═O bonds at the core/alkyl monolayer interface. We can discount the first possibility because no evidence of such a bimodal size distribution is present in probe microscopy or TEM studies [12]. The mean size resulting from electrochemical etching would be expected to depend on the applied current density, which controls the pore size and pore-wall thickness; therefore, a narrow size distribution is quite expected. The second possibility is much more likely because the previous Fourier transform infrared (FTIR) [6] and photoemission spectroscopy [12] data show that there is a small amount of oxide present in the samples. The work of others [48,50] also supports this interpretation. When nanocrystalline Si is oxidized, the Si–Si or Si–O–Si bonds are likely to weaken or break in many places because of the stress at the Si/SiO_2 interface [8]. A Si═O double bond is likely to be formed and stabilize the surface, since it does not require a large deformation energy. Such bonds have been suggested at the Si/SiO_2 interface [8]. In the literature [54], the PL emission from pure bulk silica is at 2.8 eV (442 nm), which is close to the blue peak from the alkylated samples at 430 nm. Sham *et al.* [55] measured X-ray excited optical luminescence (XEOL) and X-ray emission spectroscopy (XES) on silicon nanowires and showed that the blue emission is associated with the silicon oxide layer on the samples employed. This suggests that the blue PL emission we see is from oxidized Si species and the orange PL emission originates from unoxidized Si.

The further evidence for this interpretation could be obtained by acquiring excitation spectra with the detection wavelength set at 420 nm for blue emission, with a range of excitation energies from 5.1 to 23 eV. The blue emission was greatly enhanced when the excitation energy exceeded 8.7 eV which is the threshold energy for photogeneration of self-trapped excitons in SiO_2 [54]. **Figure 9** shows the ratio of the intensity of the blue emission to the orange emission at 8 K as a function of excitation energy in the range from 5.1 to 23 eV. Finally, using published computations of the optical gap for alkylated Si NCs [56] and Si NC size estimate of *c.* 2.2 nm, the orange emission peak could be assigned to the bandgap transition.

Many semiconductor NCs, including Si NCs, are known to show a luminescence intermittency (aka blinking behavior, see Section 1.16.4) and this is commonly discussed in terms of a mechanism in which the NC ionizes and the hole in the Si core provides an efficient nonradiative decay pathway for subsequent excitons [14]. The ionization may be thermal or Auger-assisted, although it is not known in

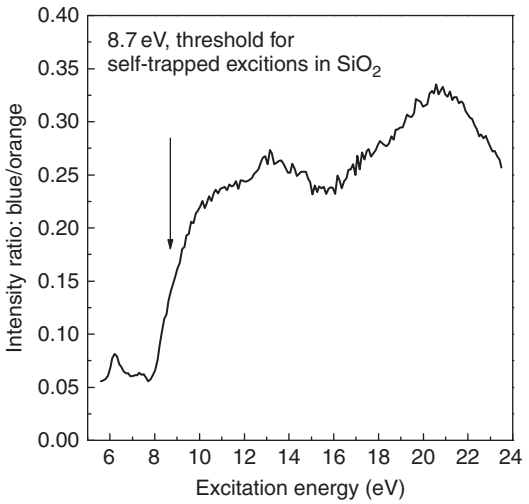

Figure 9 Ratio of blue:orange emission intensity at 8 K as a function of excitation energy between 5.1 and 23 eV; the blue emission appears at excitation energies greater than 8.7 eV which is the threshold energy of photogeneration of self-trapped excitons in SiO_2. From Chao Y, *et al*. (2006) Optical luminescence from alkyl-passivated Si nanocrystals under vacuum ultraviolet excitation: Origin and temperature dependence of the blue and orange emissions. *Applied Physics Letters* 88(26): 263119.

general whether the electron is ejected from the particle or resides in a trap state at the surface. This ionization process has been the subject of several recent theoretical studies because the photobleaching behavior is typically observed to follow a power law rather than a simple exponential decay in time [57–59]. An explanation of the temperature dependence of the luminescence of porous silicon based on a similar mechanism has also been provided; the steady-state intensity-temperature data can be fitted by an equation based on the competition between a phonon-mediated radiative decay that shows normal Arrhenius temperature dependence and ionization of the excited state through a tunneling process at finite temperature which has a Berthelot-type temperature dependence, $\exp[T/T_B]$ [44,60]. This model was successfully fitted to experimental data for the temperature dependence of luminescence from porous silicon [61,62]. The experimental data generally shows a maximum as a function of temperature that varies between ~50 and 150 K in different samples [46,61–63].

In order to investigate the detailed temperature-dependent behavior of Si NCs further, temperature quenching spectra were obtained by Chao *et al.* [64] with 21 eV excitation energy as the temperature was increased at a rate of 15 K min^{-1} (**Figure 10**). The monochromator for the detector, a photomultiplier tube (PMT), was set at blue and orange wavelengths, 420 ± 10 nm (blue) and 610 ± 10 nm. To ensure that the data obtained reflected the temperature

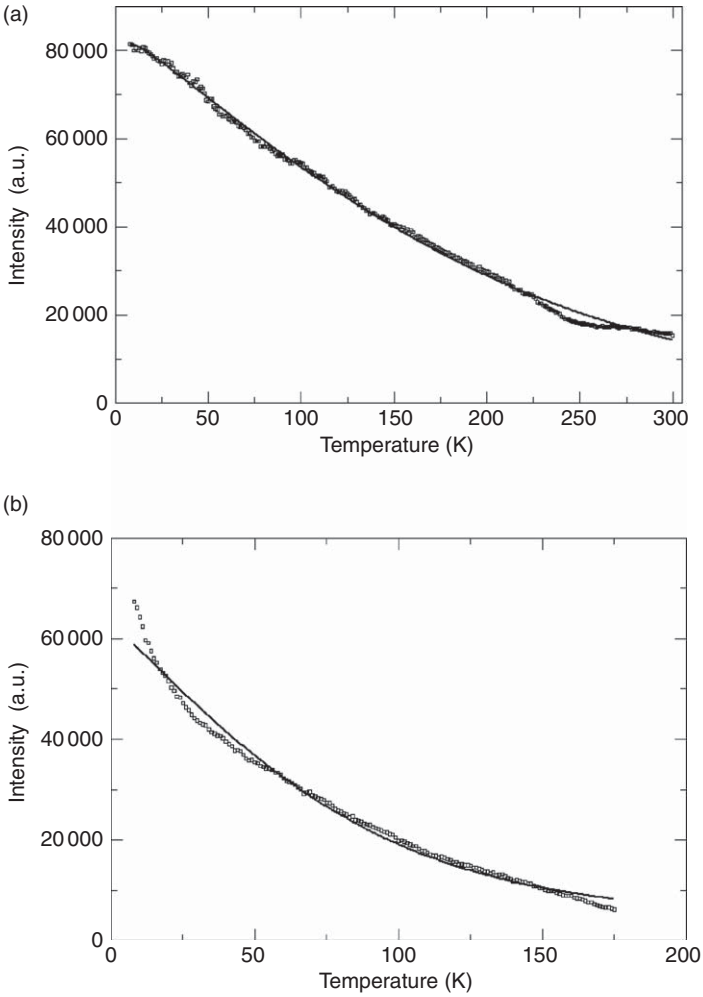

Figure 10 Evolution of the intensity of (a) orange, 610 ± 10 nm and (b) blue, 420 ± 10 nm photoluminescence (PL) bands over the temperature range of 8–300 K. The solid line is a least square fit of equation 8 to the data. From Chao Y, *et al*. (2006) Optical luminescence from alkyl-passivated Si nanocrystals under vacuum ultraviolet excitation: Origin and temperature dependence of the blue and orange emissions. *Applied Physics Letters* 88(26): 263119.

dependence of the steady-state luminescence and not a time-dependent change due to bleaching by continuous exposure to the excitation light, the peak intensities from spectra at six fixed temperatures (**Figure 8**) were confirmed to lie on the temperature sweep shown in **Figure 10**.

The emission intensities of both bands decay monotonically as the temperature increases (**Figure 10**). The blue emission was not detectable above the background signal when the temperature was higher than 175 K. The solid line is the fit to the data with equation 8.

In contrast to observations on porous silicon, the orange emission of the alkylated Si NCs shows no intensity maximum down to the lowest temperature (8 K) accessible in the experiment. The orange emission data <225 K is well described by

$$\frac{I(T)}{I_0} = \frac{1}{1 + 0.76 \cdot \exp\left(\frac{T}{T_B}\right)} \tag{10}$$

with a Berthelot temperature, $T_B = 117$ K. The origin of the dip in the orange PL at 250 K is not clear. The quenching of the blue emission is not well described by the model given in Refs. [44,60].

Both peak positions are shifted to longer wavelengths as the temperature increases from 8 K to room temperature: the orange peak position shifts from 600 ± 2 to 630 ± 2 nm. This is resulted from population of localized tail states formed by the disordered potential at the surface [45] due to the surface roughness and variations in surface stoichiometry.

In summary, there are intense blue and orange emission bands upon VUV excitation of alkylated Si nanocrystallites in a steady-state PL experiment. The blue band is only detectable at lower temperatures (<175 K) with higher excitation energies (>8.7 eV). The two emission bands originate from oxidized Si (blue) and unoxidized Si atoms (orange). The temperature dependence of the orange luminescence is well fitted by equation 8 in which the radiative decay competes with a temperature-dependent tunneling process.

1.16.4 Photobleaching and Recovery

Semiconductor NCs exhibit luminescence intermittency under continuous wave (cw) irradiation whereby the light emitted by a single NC switches off and on in a random manner, the phenomenon being termed as 'blinking'. The luminescence intermittency of semiconductor NCs irradiated by low-intensity, cw light is generally interpreted in terms of photoionization of the optically accessible excited state $|1\rangle$, either by thermal or by Auger autoionization, to generate a charged state $|2\rangle$ which itself does not luminesce because of efficient nonradiative loss [65]; rather, $|2\rangle$ discharges when the separated electron–hole (e–h) pair created by autoionization recombines to regenerate either of the neutral states $|0\rangle$ or $|1\rangle$. Following the suggestion of Efros and Rosen [65], it is assumed here that charge neutralization of $|2\rangle$ results in $|1\rangle$, which subsequently undergoes fast vibrational relaxation to $|1'\rangle$. The bright state $|1'\rangle$ decays radiatively to $|0\rangle$, by emission of a photon at a wavelength longer than that of the initial $|1\rangle \leftarrow |0\rangle$ photoabsorption. The relevant photophysical processes are summarized by the scheme

$$|0\rangle + n\hbar\omega \overset{W}{\Longleftrightarrow} |1\rangle \xrightarrow{\tau_a} |2\rangle \xrightarrow{\tau_{eh}} |1\rangle \tag{11a}$$

$$|1\rangle \rightarrow \left|1'\right\rangle \xrightarrow{\tau_r} |0\rangle \tag{11b}$$

which is a simplified and amended version of the mechanism of random telegraphing proposed by Efros and Rosen [65]. Here, W denotes the rate of n-photon absorption and stimulated emission, τ_a and τ_{eh} are the characteristic decay times for autoionization and neutralization, and τ_r represents the radiative lifetime of the photoluminescent state $|1'\rangle$ generated by $|1\rangle$. Not included in equation 11, in contrast to the mechanism noted in Ref. [65], is further photoexcitation of $|2\rangle$ by the incident light because it is not expected to produce luminescence [14]. The rates of radiative decay and photon absorption at the intensities used here are 5–6 orders of magnitude larger than the rates $1/\tau_a$ and $1/\tau_{eh}$ of the ionization and reneutralization processes of interest here. Previous studies of the radiative decay of excited states of Si NCs have measured lifetimes on the order of μs [66] or shorter [29]. In the experiments on Si NCs, the luminescence decays under CW rather than pulsed irradiation: therefore, it is not concerned with the rate at which $|1'\rangle$ decays radiatively, but rather that at which the optically excited state $|1\rangle$ is lost by other processes such as electron transfer or photochemical reactions. We do not specify in equation 11a how many photons are absorbed to reach the $|1\rangle$ state and leave open questions concerning the precise electronic structure of $|1\rangle$ and $|1'\rangle$.

A simple treatment of the rates of pair occupation of the NC states based on the mechanism of equation 11 can be made based on the premises that the

applied light field rapidly establishes an equilibrium between $|0\rangle$ and $|1\rangle$, whose occupation probabilities are $P_0(t)$ and $P_1(t)$, and that autoionization and electron–hole recombination take relatively far longer by comparison. Likewise, vibrational relaxation of $|1\rangle$ to the emitting state $|1'\rangle$ is assumed to occur over a time scale much shorter than τ_a, τ_{eh}, and τ_r. The slow time rate of change of $P_1(t)$ is then

$$\frac{dP_1}{dt} = -\frac{P_1}{\tau_a} + \frac{P_2}{\tau_{eh}} \tag{12}$$

with the assumption that $\tau_r << \tau_{eh}$, τ_a. Setting $dP_1(t)/dt = 0$ in the limit $t \to \infty$, the ratio of neutral to charged NCs at steady-state is then

$$\frac{P_0(t \to \infty)}{P_2(t \to \infty)} = \frac{\tau_a}{f[I(\lambda);\lambda]\tau_{eh}} = \frac{I_\infty}{I_0 - I_\infty} \tag{13}$$

where I_∞ and I_0 designate the PL intensity in the limits $t \to \infty$ and $t = 0$, respectively. In the limit $t \to \infty$, the fraction

$$f[I(\lambda);\lambda] = \frac{P_1(t \to \infty)}{P_0(t \to \infty)}$$

is an increasing function of intensity $I(\lambda)$ and, for the Si NCs studied here, a decreasing function of wavelength between 488 and 725 nm. Under conditions of low-intensity irradiation such that saturation of the $|1\rangle \leftarrow |0\rangle$ transition is avoided, $f[I(\lambda); \lambda] << 1$ and $P_0(t)/P_2(t)$ is proportional to $P_{1'}(t)/P_2(t)$. Although it is not possible to make direct measurements of the value of $f[I(\lambda); \lambda]$ because of the difficulty of determining reliably the fraction of emitted light collected by the detection optics, the analysis of the experimental PL intensity in terms of equation 13 presented in Section 1.16.4.1 indicates that $f[I(\lambda); \lambda]$ remains small at all times $0 \leq t \leq 300$ s; in the experiments reported in Ref. [67], the condition $t \to \infty$ is reached about 200 s after $t = 0$. The authors of Ref. [65] used a sequence of random numbers to simulate the stochastic behavior of light emission from a single NC; the kinetic approach leading to equation 13 suffices to account for the temporal dependence of luminescence from a macroscopic ensemble of NCs.

1.16.4.1 Bleaching and Recovery of PL

Figure 11(a) is the time-dependent luminescence showing the decay of intensity $I(\lambda; t)$ from a peak I_0 upon irradiation to a finite steady-state value I_∞ and partial recovery of intensity after a period during which the excitation source is extinguished. Red line: $\lambda = 488$ nm excitation, 10 s recovery time. Green line: $\lambda = 488$ nm excitation, 60 s recovery time. Blue line: $\lambda = 633$ nm excitation, 60 s recovery time. Relative to the red curve, the green and blue intensity traces are displaced in time by +25.0 s and the green trace is displaced upwards in intensity by 0.5 arbitrary units for clarity. The incident laser intensities at $\lambda = 488$ (632) nm are of 0.30 ± 0.01 (0.25 ± 0.01) kW cm^{-2}. At a given incident laser power, the intensity of luminescence intensity is greater under irradiation at 488 nm by a Ar ion laser than at 633 nm by a HeNe laser because the absorption coefficient of the Si NCs increases at shorter wavelengths [6]. When the CW laser light is first incident on the NCs, a large initial PL

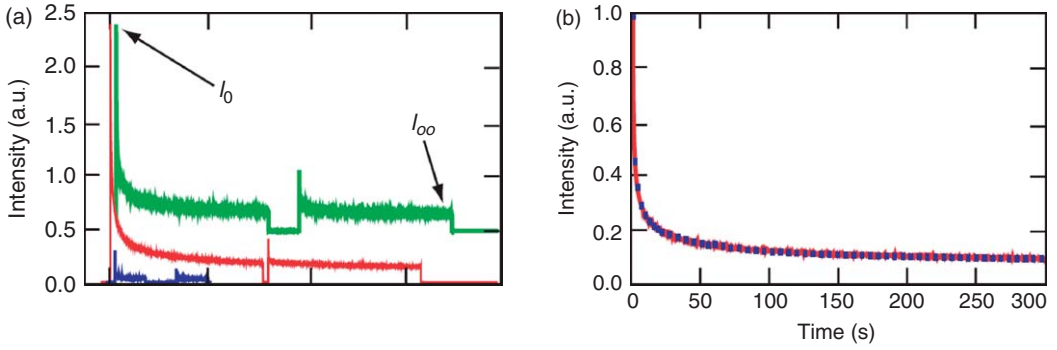

Figure 11 (a) Time-dependent luminescence showing the decay of intensity $I(\lambda; t)$ from a peak I_0 upon irradiation to a finite steady-state value I_∞ and partial recovery of intensity after a period during which the excitation source is extinguished. Red line: $\lambda = 488$ nm excitation, 10 s recovery time. Green line: $\lambda = 488$ nm excitation, 60 s recovery time. Blue line: $\lambda = 633$ nm excitation, 60 s recovery time. (b) Fit of $I(t)$ recorded at $\lambda = 488$ nm to equation 14: the data are shown in red as in (a) and the fit as blue squares. From Rostron RJ, Chao Y, Roberts G, and Horrocks BR (2009) Simultaneous photocharging and luminescence intermittency in silicon nanocrystals. *Journal of Physics: Condensed Matter* 21: 235301.

intensity I_0 is observed which decays to a steady-state value I_∞ as $t \to \infty$: an irradiation time of approximately 300 s is sufficient to reach steady state at $\lambda = 488$ nm and about 80 s at $\lambda = 633$ nm. The ensemble of NCs appears to photobleach when exposed to low- intensity CW light because the ratio $P_2(t)/P_1(t)$ of charged (dark) to neutral (bright) NCs increases until a steady state is reached where the rates of autoionization and electron–hole recombination are balanced. The bleaching of PL is more marked at the shorter wavelength where I_∞ reaches a level $I_\infty \simeq I_0/9$. However, after a recovery time of 10 or 60 s in the absence of irradiation, the PL intensity partially recovers when irradiation recommences. The recovery may be expressed as the fractional excess of the initial peak area compared to the steady-state value integrated over the following 300 s of irradiation, that is,

$$\int_0^{300} \frac{I(t) - I_\infty}{I_\infty} \cdot \mathrm{d}t$$

this quantity is proportional to the fraction $P_1'(t)/P_0(\mathrm{t} = 0)$ of particles in the uncharged, emissive state $|1'\rangle$ and could be determined more precisely than the value of intensity at any particular point in time. The extent of recovery increases as the time for charge neutralization is increased. Direct evidence that PL bleaching is caused by a physical process rather than a chemical reaction is provided by an examination of PL spectra at different times during the period of their decay. **Figure 11(b)** shows the fitting of $I(t)$ recorded at $\lambda = 488$ nm to equation 14: the data are shown in red as in (a) and the fit as blue squares; for clarity, only every 50th fitted point is displayed. The mean first-order decay time is $\langle\tau\rangle \simeq \tau_a = 1.08 \pm 0.03$ s, $\gamma'_a = 4.07 \pm 0.04$ and the ratio of steady-state to initial PL is $I_1/I_0 = 0.086 \pm 0.001$. The reduced chi-squared value of the fit is $\chi^2_r = 1.016$. **Figure 12** shows the spectral dependence of the luminescence shown in **Figure 11(a)** at the onset of irradiation, after 90 s and after 300 s, when $I(\lambda; t)$ has nearly reached its steady-state limit. The spectra are essentially identical after normalization with respect to the peak intensities. This result is consistent with the interpretation that the luminescence bleaching process results in a fraction of NCs which cease to emit light, that in the absence of irreversible chemical changes, for example, oxidation of charged NCs, luminescence spectra recorded at the start of irradiation ($t = 0$) and at steady state ($t \to \infty$) should be the same except for a scale factor, and that the intermittency should be reversible.

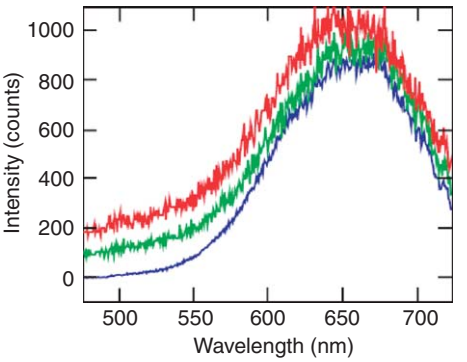

Figure 12 Photoluminescence spectra recorded at 0 (blue), 90 (green), and 300 (red) s after the start of irradiation of alkyl Si NCs by 0.30 ± 0.01 kW cm^{-2} light at $\lambda = 488$ nm. The spectra recorded at $t = 90$ and 300 s have been shifted upward by 100 and 200 counts and multiplied by 11 and 17, respectively to facilitate comparison. From Rostron RJ, Chao Y, Roberts G, and Horrocks BR (2009) Simultaneous photocharging and luminescence intermittency in silicon nanocrystals. *Journal of Physics*: *Condensed Matter* 21: 235301.

1.16.4.2 Dispersed Kinetics of Luminescence Bleaching and Recovery

The present analysis of data such as those displayed in **Figure 11(a)** is based on the mechanism given by equation 11 with the interpretation that the characteristic decay times τ_a and τ_{eh} are randomly distributed about mean values due to the heterogeneity of NC size in the sample. It is possible to fit these curves by a sum of exponentials, but it is preferable to interpret the bleaching in terms of a single exponential with a single, characteristic decay time distributed about a mean value [68] for two reasons: first, this approach invokes fewer fitting parameters than even a double exponential fit, whereas at least three exponentials are required to achieve a fit of comparable quality; and second, the physical significance of the lifetimes in such a tri-exponential fit is not so apparent [69]. Adopting the notation of Ref. [70], the intensity of PL at time t may be written as

$$I(t) = \frac{I_0}{\sqrt{\pi}} \int_{-\infty}^{\infty} \exp[-t/\tau - x^2]\mathrm{d}x \qquad (14)$$

where $\tau = \langle\tau\rangle \exp[-\gamma x]$ and the Gibbs energy of activation is distributed around its mean value as $\Delta G^{\ddagger} = \Delta G_0^{\ddagger} + \gamma x RT$. It is not unreasonable that there be a distribution of rates because there is a distribution of particle sizes [71] and the potential energy required to charge NCs depends inversely on their radius according to Gauss' law. **Figure 11(b)**

displays a single-exponential fit to the data $I(t)$ shown in **Figure 11(a)** obtained when the NCs are irradiated at $\lambda = 488$ nm. Equation 14 provides a reasonable fit to the time-dependence of PL intensity. According to equations 12 and 14, the mean first-order decay time extracted from the time-dependent PL data is

$$\langle \tau \rangle = \left\langle \frac{1}{\tau_a} + \frac{1}{f[I(\lambda);\lambda]\tau_{eh}} \right\rangle^{-1}$$

However, we may approximate $\langle \tau \rangle$ as $\langle \tau_a \rangle$ because $\langle \tau_a \rangle \ll f[I(\lambda);\lambda]\langle \tau_{eh} \rangle$ (see below). Values of the parameters extracted from the fit given in **Figure 11(b)** are $\langle \tau_a \rangle = 1.08 \pm 0.03$ s and $I_\infty / I_0 = 0.086 \pm 0.001$. A large dispersion parameter $\gamma_a = 4.07 \pm 0.04$ was obtained from the fit, but this is anticipated by the dependence of the electrostatic contribution to the activation energy on particle size. It may be concluded that the simple reaction scheme of equation 11 provides a satisfactory description of the PL bleaching process, but that the time constant for autoionization should be treated as a random variable with a distribution determined by variations in particle size and local environment throughout the sample.

If a sample of Si NCs is irradiated until the PL reaches a steady state, the majority of the particles at the focal point of the microscope will be charged if $\langle \tau_{eh} \rangle \gg \langle \tau_a \rangle$. In the absence of laser light, the only process occurring is electron–hole recombination and the fraction of initial PL intensity recovered when laser irradiation is recommenced for a further 5 min can be used to determine a value for the mean lifetime $\langle \tau_{eh} \rangle$. **Figure 13** shows the recovery of PL intensity following this procedure; from these data the first-order rise time for electron–hole recombination was determined as $\langle \tau_{eh} \rangle = 770 \pm 300$ s with a dispersion parameter $\gamma_{eh} = 4.7 \pm 0.6$ and the fraction of luminescence intensity regained by further laser irradiation is 0.85 ± 0.03. These data also indicate that the process responsible for PL bleaching is substantially reversible and therefore unlikely to be due to a photochemical process.

A quantitative estimate of the value of $f[I(\lambda);\lambda]$and a check on the consistency of the analysis of **Figures 11(b)** and **13** can be made by comparing the measured ratio $I_\infty/(I_0 - I_\infty)$ with equation 13 subject to a minor modification to take account of the distribution of decay times. If $\langle \tau_{eh} \rangle$ and $\langle \tau_a \rangle$ are distributed according to $\langle \tau_a \rangle \exp[\gamma_a x]$ and $\langle \tau_{eh} \rangle \exp[\gamma_{eh} x]$, respectively and it is assumed that the lifetimes are slower or faster than average for

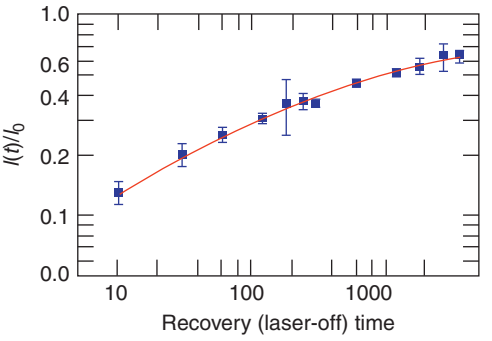

Figure 13 Fractional recovery of photoluminescence (blue squares with error bars) following a prior exposure time of 300 s and fit based on equation 14 (red curve). The mean first-order rise time describing the recovery of luminescence is $\langle \tau_{eh} \rangle = 770 \pm 300$ s; the parameter describing the spread of the distribution is $\gamma_{eh} = 4.7 \pm 0.6$; and the fraction of recovered luminescence intensity is $\int_0^{300} [I(t) - I_\infty]/I_\infty \cdot dt = 0.85 \pm 0.03$. From Rostron RJ, Chao Y, Roberts G, and Horrocks BR (2009) Simultaneous photocharging and luminescence intermittency in silicon nanocrystals. *Journal of Physics: Condensed Matter* 21: 235301.

both processes and not slow for one and fast for the other, so that a common variable x may be employed to calculate the mean of their ratio, then equation 13 becomes

$$\frac{I_\infty}{I_0 - I_\infty} = \frac{\langle \tau_a \rangle}{f\langle \tau_{eh} \rangle} \exp\left[(\gamma_{eh} - \gamma_a)^2/4\right] \qquad (15)$$

Substituting values of $\langle \tau_a \rangle$, $\langle \tau_{eh} \rangle$, a and eh extracted from the fits to **Figures 11(b)** and **13** we obtain $f[I(\lambda);\lambda] = 0.016 \pm 0.012$ and $(f[I(\lambda);\lambda]\langle \tau_{eh} \rangle)^{-1} = 0.08 \pm 0.12\ s^{-1}$. The error introduced by the assumption $\langle \tau_a \rangle^{-1} \ll (f[I(\lambda);\lambda]\langle \tau_{eh} \rangle)^{-1}$ in the analysis of the bleaching data, as shown in **Figure 11(b)**, is therefore 0<8<20% of the value of $\langle \tau_a \rangle^{-1}$, which may be regarded as acceptable in view of the simplicity of the least-squares fitting procedure invoked to analyze the experimental data in terms of a single, Gaussian-distributed decay time. We note that not only the value of $f[I(\lambda);\lambda]$ is subject to a large uncertainty, but also the value of this quantity is not required for the physical interpretation of the above results.

In summary, the bleaching of luminescence of a film of alkyl-capped Si nanocrystals (alkyl-Si NCs) subject to CW irradiation by laser light at $\lambda = 488$ or 632 nm is found to be essentially entirely reversible over timescales up to 5 min, which suggests that suppression and recovery of luminescence are due to an electron-transfer process rather than an irreversible chemical change. The intermittency of

luminescence can be described by a sequence of photoabsorption, autoionization, and electron–hole recombination steps, which is a simplified version of the model presented by Efros and Rosen [65]. Mean lifetimes of $<\tau_a> = 1.08 \pm 0.03$ s $<\tau_{eh}> = 770 \pm 300$ s are determined for autoionization of Si NC excited states and electron–hole recombination, respectively, when allowance is made for a Gaussian distribution of decay times due to a distribution of particle sizes and compositions.

1.16.5 X-Ray Absorption Spectroscopy and XEOL

X-ray absorption spectroscopy (XAS) is a powerful structural technique to investigate the short-range environment around selected atomic species in condensed matter. While scanning the X-ray energy impinging onto the sample, a core-level photoelectron is generated. This is scattered by the surrounding matter producing interference effects visible in the absorption cross section and usually referred to as X-ray absorption fine structure (XAFS). Near-edge X-ray absorption fine structure (NEXAFS), which is also sometimes referred to as X-ray absorption near edge structure (XANES), typically represents the energy region from the absorption edge to about 50 eV above the edge. NEXAFS spectra provide important information about the electronic and structural properties [72]. The process itself is general and therefore fundamental to study structural properties in materials such as

- liquids, molecular solutions, liquid crystals;
- single- and poly-crystalline materials;
- amorphous and highly disordered solids; and
- molecules and macromolecules containing metallic atoms or partially substituted with heavy atoms.

The potential utilization of near-edge features for the structural determination of matters was first recognized in 1920 by Kossel [73]. However, research effort in this area was limited primarily due to difficulties in obtaining intense light sources for excitations and due to the complexity in data analysis. During the 1970s, the availability of bright, polarized, and tunable synchrotron light sources, as well as the development of scattering theories for the interpretation of near-edge features, made XAFS a powerful tool for structural determinations. By the mid-1980s, NEXAFS had become a powerful surface spectroscopy, especially in elucidating the electronic and structural properties of molecules on surfaces [72].

The absorption of an X-ray photon, with a resonance energy $h\upsilon$, gives rise to an electronic excitation from the core level to an unoccupied state. As shown in **Figure 14**, a core hole is created as a result of the resonance excitation. In NEXAFS measurements, the resonance transition is measured by following the annihilation, instead of the creation, of core holes. The energy gained by annihilation can be released by either the radiation of fluorescence photons or by the emission of Auger electrons. In this process, photoelectrons are always there; thus, the ejected electrons include photoelectrons and Auger electrons. NEXAFS spectra can be recorded by measuring either the electron yield or fluorescence yield as a function of incident photon energy (**Figure 15**).

The X-ray absorption spectra of gaseous materials can at least in principle be measured in transmission mode, recording the changes in the 'transparency' as a function of the incident photon energy: Due to the extremely short attenuation lengths of soft X-rays in solids, this is not possible in solids (except possibly in some cases for ultrathin films). Instead, the incident photon energy dependence of the yield of secondary particles (electrons or photons), which are produced during the decay of the core excitation, can then be used in order to get information on the energy dependence of the absorption cross section [72]. For practical reasons, these techniques are favored even when recording gas-phase NEXAFS, and due to the relatively longer escape depths of photons,

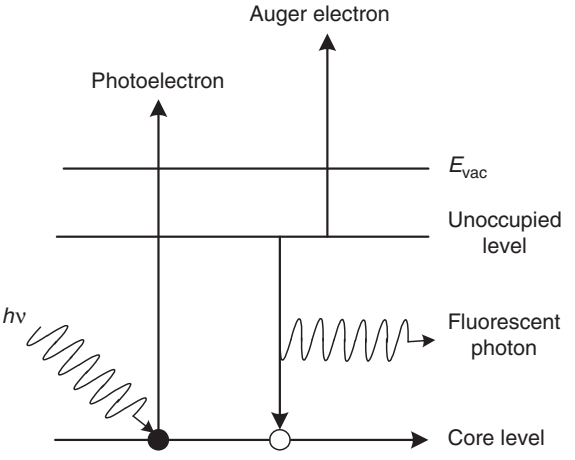

Figure 14 Schematics of creation and annihilation of a core hole as a result of X-ray absorption.

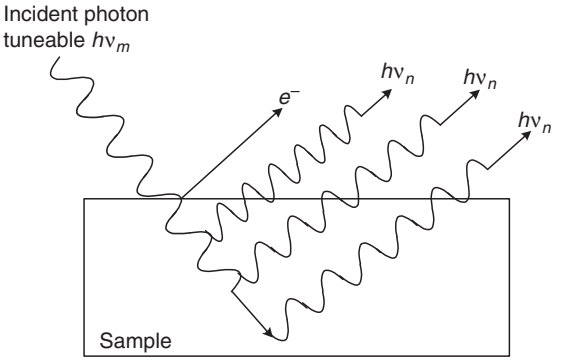

Figure 15 Near-edge X-ray absorption fine structure (NEXAFS) measurements are carried out by following the de-excitation process, which generates either an Auger electron or a fluorescence photon.

the photon yield measurements can also be used on liquids.

To obtain an experimental spectrum which is more or less directly corresponding to the absorption cross section, total or partial electron or photon yields can be recorded. These different options generally use different detectors, and have advantages and limitations, which are reviewed below. First, total electron yield (TEY) can be obtained most simply by recording the sample drain current, as electrons are photoemitted from the sample upon interaction with incident light either directly or due to decaying of an autoionizing state. The drain current setup essentially consists of a wire, which connects the sample holder, isolated from the ground, through a vacuum feed-through to a pico-amp meter. An obvious advantage of this technique is the simplicity of the setup, while the results for metallic or even semiconducting samples are nevertheless as good as for the more sophisticated setups. However, applicability to conducting samples only and the shallowness of the surface layer of the sample that is probed can sometimes make it necessary to use a different setup. Other possibilities for recording the TEY signal are to use a channeltron detector or a multichannel plate (MCP).

Second, the total photon yield, alias total fluorescence yield (TFY) signal can be recorded by using a channeltron detector, an MCP detector or, as a less-efficient option, by using the X-ray emission (XE) spectrometer in zero-order diffraction. Being a photon-in–photon-out technique, this method can reach considerably larger probe depths (on the order of 1000Å) and is less sensitive to possible surface contamination. It can also be used to measure absorption in buried layers (e.g., in samples covered by a layer of material protecting the sample from oxidation during transfer).

When using this technique, however, one should be careful considering the effects of self-absorption, and the fact that the absorption cross section, in many cases, need not be proportional to the photon yield signal. The effect of self-absorption is illustrated in **Figure 16**. For a bulk sample or a thick film, all of the incoming light gets absorbed, although the effective absorption length depends on the energy-dependent cross section. If the TFY signal is then recorded at a near-normal (exit) angle, the secondary photons come from different depths in the sample for different incident energies, but due to the long escape depth these photons are still capable of leaving the sample and the dependence of the total number of emitted photons, in the extreme case, can be constant (independent of energy and only dependent of the incident intensity). The best way to prevent this from happening is to use near-normal incidence angles and grazing exit angles, so that photons emitted only from a thin surface layer are detected. This signal should then be proportional to photons absorbed in the same layer of limited thickness, and the total number of the absorbed, and emitted, photons should be proportional to the absorption cross section. The amount of self-absorption differs from material to material between the extremes of a flat line (constant) in the spectrum to negligible

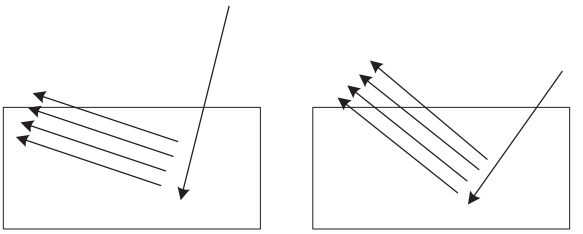

Figure 16 Saturation effect in total fluorescence yield (TFY) (absorption) spectroscopy: due to the large photon escape depth, the photon yield recorded with near-normal exit angles may at different energies (for different energy-dependent absorption cross sections) contain contribution from different depths in the sample, neutralizing the effect of the absorption cross section. At near-normal detection angles, the light at energies with smaller absorption coefficient can originate from deeper in the sample than at energies with large absorption cross section. The total intensity observed can at the same time be almost constant. From Käämbre T (2002) *Resonant Soft X-ray Spectroscopic Studies of C60 and Related Materials.* Doctoral thesis, Comprehensive Summary, Physics. Uppsala: Acta Universitatis Upsaliensis.

effects. The technique can still be very useful, especially in the cases when this is the only option, for example, for buried layers or liquids in a containing cell quipped with a window [74].

Third, partial electron yield (PEY) can be measured using a photoelectron spectrometer and choosing an energy window (and integrating the total count rate within the window). This will give the decay rate through a certain transition. A less sophisticated alternative to this is to use a total yield detector in combination with one or several retarding grid(s) in order to set a low kinetic energy limit for the electrons which can reach the detector. Using the PEY, instead of TEY, enables one to enhance the element specificity to some extent (in case of a composite sample) and gives some flexibility to choose the probe depth by recording decay channels with quite different kinetic energies.

Fourth, partial fluorescence yield (PFY) measures the decay rates (of an energy-dependent magnitude of a core-excited population) through a specific fluorescent decay channel. Although this technique usually suffers from extremely low count rates, the capability to discriminate more strictly against (the approximately constant background) fluorescence from other elements in a composite sample make it in certain cases useful. The signal can be detected by choosing a suitable energy window in the spectrometer and integrating the count rate for each incoming photon energy step [75].

1.16.5.1 XAS of Silicon Nanostructures

Figure 17 is a typical XAS taken at Si $L_{2,3}$ region from porous silicon. Two edges at 100 and 104 eV, corresponding to Si and SiO_2, respectively, imply that Si—Si and Si═O bonds are present in the sample.

NEXAFS spectroscopy measurements have been performed on both bulk Si and Si NCs. The principal aim was to observe the changes in the absorption features due to quantum confinement in the Si NCs when compared to bulk Si. NEXAFS uses excitation of a core electron to the unoccupied molecular orbitals (MOs), yielding important information on the electronic structure involving chemical shifts as well as the fine structure of the unoccupied levels. Thus, both chemical shifts and fine structures are sensitive to chemical bonding and correlate with the electron transport mechanism [76,77].

NEXAFS measurements using partial photon yield absorption as conventional electron yield suffer

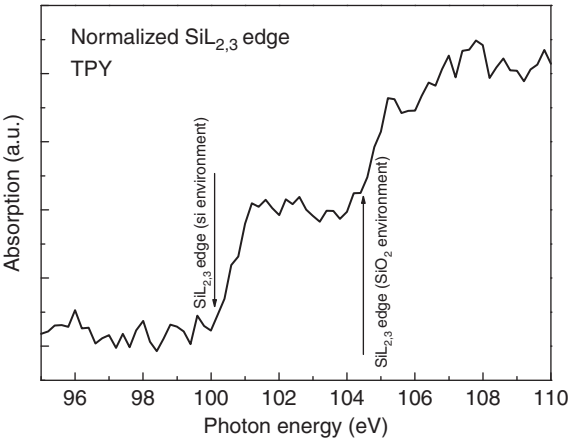

Figure 17 Si $L_{2,3}$ region total photon yield near-edge X-ray absorption fine structure (NEXAFS) spectrum, two edges at 100 and 104 eV, corresponding to Si and SiO_2, respectively, which implies that Si–Si and Si–O bonds are present in the sample.

two drawbacks: (1) due to the porosity of the porous silicon formed during the etching process [6], the structures in the NCs are not well connected electrically and the energy of the electron detected by photoemission is influenced by the charge buildup during the measurement, thus electron yield is hampered by surface charging effects, whereas total photon yield which is insensitive to surface charging can be used to map the unoccupied states; and (2) photon yield is also bulk sensitive. The penetration depth is 60 nm or more when compared to electron yield which is around 5 nm [78,79].

Figure 18 shows the PEY obtained from bulk Si (spectrum (a)) and passivated Si NCs (spectrum (b)) at the Si $L_{2,3}$ edge. Data for bulk silicon are in agreement with previous work [80,81]. However, the absorption spectrum from the NCs is remarkably different from both the bulk and what would be expected from a consideration of the theoretically determined unoccupied density of states (DOS) in silicon clusters containing a few tens of atoms [82, 83]. The NC XAS consists of a single, relatively sharp, spin–orbit split peak superimposed upon a smooth background intensity between threshold and the onset of oxide-related absorption (bands at 106, 108 eV and a weak band at 115 eV which are commonly attributed to inner well resonances of Si oxide [81,84–86]). The relatively high strength of the oxide features in the XAS spectra of the Si NCs despite the bulk-sensitive PPY detection can be attributed to the structure of the NC film: passivation of the Si NC

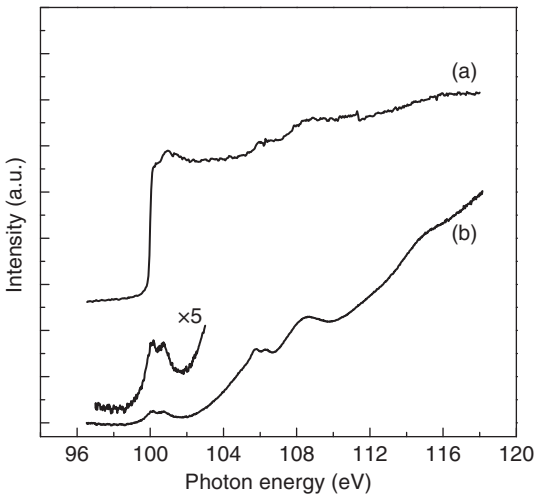

Figure 18 Comparison of absorption features of (a) bulk silicon and (b) silicon quantum dots at the vicinity of the Si $L_{3,2}$ edge by the partial photon yield (PPY) technique. From Šiller *et al*. (2009) Core and valence exciton formation in x-ray absorption, x-ray emission and x-ray excited optical luminescence from passivated Si nanocrystals at the Si L-2,3 edge. *Journal of Physics*: *Condensed Matter* 21: 095005.

surfaces by alkyl groups prevents their sintering, thus the film consists of individual nanoparticles each with their own surface (including suboxides) distributed throughout the bulk of the film. Therefore, in contrast to a bulk silicon sample with the same surface composition, a film of Si NCs with (limited) surface oxidation presents surface oxide throughout the film thickness, thus increasing the oxide signal relative to a conventional solid silicon sample. A broadening of absorption onset was observed by Eisebitt *et al.* [87,88] in XAS from porous Si, and attributed to the crystallite size distribution in their samples. However, in the spectra shown in **Figure 18**, which are from a sample with a well-defined and narrow diameter distribution [71], a clear 0.61 eV spin–orbit splitting [89] is observed in the PPY from the NCs (magnified region of **Figure 18**, curve b), while such splitting may be washed out by the size inhomogeneity in the porous Si crystallites [87,88].

Single-dot luminescence spectroscopy has been used to study the emission line width of individual Si NCs and these studies have confirmed that oxidized NCs exhibit discrete energy levels rather than continuous bands [90]. Therefore, the simple quantum mechanical model of 'particle in the box', leads one to expect the increased the level spacing in NCs compared to bulk and therefore the transition from Si L_2 and L_3 levels to the lowest excited state should be better resolved than in the bulk Si.

Although a sharp rise in X-ray absorption is observed in bulk silicon, a shallow onset has been theoretically predicted [89,91], because the absorption threshold should be related to the CB minima s-like electronic states due to dipole selection rules. The steep rise in absorption in bulk Si at the $L_{2,3}$ threshold, which is much steeper than the predicted CB DOS, has been attributed to excitonic effects in core-electron transitions to the CB, with bound core excitons being of Wannier type [92].

The theoretically calculated radius of the core exciton at the $L_{2,3}$ edge in bulk Si is ~1.6 nm [93], which agrees well with measured X-ray absorption photon yield [89,94]. The radius of the elemental Si core of the NCs studied here is, at $d/2 = 1.1 \pm 0.2$ nm [71], substantially smaller than the core exciton radius, hence X-ray absorption in the silicon core at threshold should favor an excitonic final state more tightly bound than the corresponding bulk exciton. In consequence, it is not unreasonable that core exciton formation dominates emission below the oxide edge, to a greater degree than in bulk Si, leading to an absorption spectrum which no longer directly reflects the unoccupied DOS. Indeed, the dominance of a single spin–orbit split doublet at the onset of X-ray absorption in the NCs suggests a narrow, well-defined core exciton state in this system.

In addition to gross differences in spectral shape between the XAS of bulk silicon and Si NCs, there is a small, and unexpected, apparent red shift in the absorption threshold in the NCs (located at 99.3 ± 0.1 eV) when compared with bulk Si (99.6 ± 0.1 eV). This behavior is in contrast to the blue shift that has been previously reported for porous Si [81,95], SiO_2/Si superlattices [96], and for Si nanoclusters [28] and attributed to quantum confinement. A red shift has, however, been reported for 2 and 3 nm diameter silicon clusters formed upon annealing SiO_2 superlattices by Zimina *et al.* [97], although changes in the absorption spectrum were much less pronounced than those reported here. Although no other evidence was provided to support this attribution, it was suggested that this red shift, smaller in magnitude than that observed here, was associated with core exciton formation, which would be consistent with the interpretation of the X-ray absorption spectra from Si NCs (**Figure 18(b)**) presented above.

XAS at the L_2 edge predominantly probes the NC core, but because of the small number of Si atoms in the core and their close proximity to the surface, an alternative suggestion for the red shift could be that it arises due to the presence of the surface, perhaps from some strain-induced structural relaxation. For example, a red shift has been observed for very small diamond clusters (diamondoids) [98] and it has been suggested in this case that the bulk-related unoccupied states do not exhibit any quantum confinement but they are influenced by the termination of the surface by CH and CH_2 groups.

1.16.5.2 XEOL of Si Nanocrystals

XEOL is essentially an energy-transfer event in which the absorption of the X-ray photon produces a large number of energetic electrons (photoelectron and Auger electron, (**Figure 14**)). These electrons in turn cause further ionization and excitation. The energy is transferred to luminescent centers through inelastic processes which lead to the creation of holes in the VB and electrons in the CB in semiconductor nanostructures, for example, or holes and electrons in the occupied and unoccupied MO of organic molecules, respectively. The recombination of holes and electrons will emit light. This is the well-known scintillation process [99].

The first major application of XEOL was the quantitative analysis of rare earth impurities, which was extensively carried out in the 1960s and 1970s [100]. A detection capability of 1 ppm–1 ppb was achieved for the analysis of Tb, Dy, Eu, and Gd in Y_2O_3 [101]. Considering that XEOL originates from the excitation of a core electron, a combination of XEOL detection and the energy tuneability of synchrotron radiation (SR) is promising for chemical state analysis of elements [102].

XEOL is a photon-in–photon–out technique. Using laboratory soft X-rays such as Mg Kα (1253.6 eV) and Al Kα (1486.6 eV), and visible UV and soft X-ray (10–3 keV) from a tunable synchrotron light source, it is often possible to conduct site and sampling depth selective measurement [102–104]. The sampling depth selectivity comes from the energy-dependent penetration depth of the photons and the site selectivity comes from the tuneability of the source. For example, when the photon energy is tuned to the silicon L-edge, the photon will be absorbed preferentially by the silicon atom. This channel-selective excitation will greatly facilitate the identification of the origin of luminescence [99].

The origin of the luminescence in Si NCs is debatable, and many different mechanisms have been invoked to explain the visible PL from porous Si and Si NCs [105–107]. Most of the PL can be explained by quantum-confinement mechanism [28], Si/SiO_2 multilayer quantum wells [96]. According to the extended version of this mechanism, the larger bandgap of the Si NCs is attributed to quantum-confined Si nanostructures where the recombination of electrons and holes occurs in surface states [108]. According to experimental and theoretical reports, quantum confinement in Si NCs for the observation of visible luminescence requires the size to be <5 nm [63,109]. To address all these issues and to identify exactly which site is responsible for the luminescence necessitates the use of site-selective luminescence.

XEOL is used to address the site-selective luminescence from the silicon nanocrystallites. The advantages of XEOL, using tunable soft X-ray SR as the excitation source, are its state and site selectivity [99]. The tuneability of SR makes it possible to study XEOL of a particular element or even a specific chemical state in a composite environment. Soft X rays have a short absorption length (10^2–10^3 nm) [103] comparable to typical film thickness. In a XEOL experiment, the optical spectrum can be recorded at selected incident photon energies. Additionally, the NEXAFS can be recorded in the PL yield at zero order [102,104] or at a specific wavelength. This process is called optical X-ray absorption fine structures (optical XAFS). When these three detection modes are collectively used, one can study the electronic and optical properties of Si NCs. XEOL together with optical XAFS will reflect the local structure and the electronic properties of the absorbing atom and address the site responsible for the luminescence. This technique has already shown the site specificity in Si K edge and L edge studies of porous silicon [102,103].

In the experiment described below, Si $L_{2,3}$ excitation was used to study the luminescence properties of Si NCs. At the Si K-edge Sham *et al.* [102] showed that in fresh porous silicon, the Si–Si bond is involved in the luminescence. However, the difference between the excitation of a K shell core electron and the L shell lies in the different distance over which the absorbed energy migrates before being deposited in a useful form (the generation of visible luminescence). In the case of K shell absorption, where electrons with energies in excess of 10^3 eV are involved, the distance between the primary

photoionization event and the luminescence event has been estimated to be ~30 nm; however, in the case of L shell absorption this distance is reduced to about 1 nm [110]. This indicates that the probability of recombination of the carriers in a different phase the material from the phase in which the carriers are generated, is considered to be bigger in the case of the K shell. Thus, L shell absorption is a better probe than K shell absorption to identify the luminescent center.

Synchrotron-excited luminescence of Si NCs was studied at the vicinity of the silicon L edge, which corresponds to the excitation of a 2p electron to the bottom of the CB. The luminescence was monitored with an optical monochromator, typically in the range of 200–900 nm. The luminescence which is either due to the recombination of holes in the VB with electrons in the CB, or due to defects can be monitored. The PL yield can in turn be used to record XAFSs that provide structural information for the absorption site that is responsible for the luminescence [102]. In **Figure 19** a photon energy of 145 eV is used to excite the Si NCs.

Dispersed luminescence spectra were obtained with a photon energy of 145 eV. At this energy, both the silicon core level and SiO_x were excited. The spectral shape shows the existence of three major bands at ~480 nm (2.58 eV), ~630 nm (1.97 eV), and 730 nm (1.69 eV). The blue emission band at 2.58 eV is attributed to the defects associated with SiO_x states. This 2.58 eV feature is commonly observed in silica glass and has been attributed to the triplet to the ground state luminescence from a SiO_2 defect, a bridging oxygen vacancy between two adjacent Si [8,111]. Luminescence at similar wavelengths have been observed in porous silicon and silicon nanostructures [8,12,111]. When excited above the threshold, in the case 145 eV excitation energy, both Si and SiO_x compete for the incoming photons. The absorption of oxide-related Si will facilitate the oxide chromophore if the process has high quantum yield. It is also interesting to note that this 2.58 eV (480 nm) band can originate from elemental silicon as well, since Si NCs are known to have a widely tunable range of PL [63]. This suggests that there might be an overlap of silicon oxide and silicon nanocrystallite bands contributing to the observed luminescence bands because of quantum confinement in the silicon nanocrystallites. A similar process is also reported in porous silicon [111]. The peak at 630 nm is the most intense among the three bands, and can be attributed to electron–hole recombination in silicon nanocrystallites due to quantum-confinement behavior. The weak band at 700 nm, can be attributed to the interface defects between nanocrystalline Si and silicon oxide or suboxide, or due to quantum-confined NCs of large size (>2 nm) [112]. In order to explore the site-selective luminescence it is necessary to address which site is responsible for the observed luminescence.

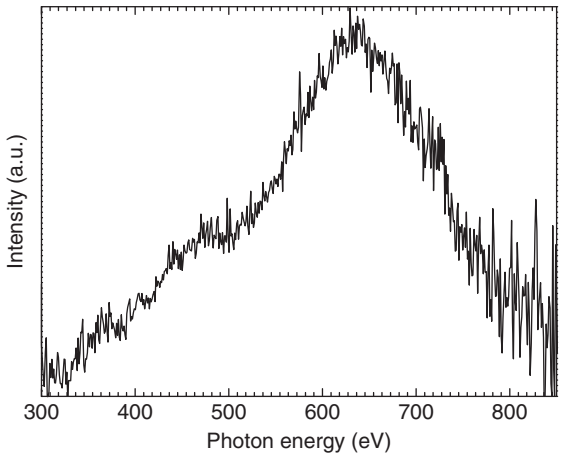

Figure 19 The photoluminescence of the silicon quantum dots obtained at 145 eV photon energy at room temperature.

1.16.6 Applications

There are many applications of porous silicon-based materials. Some of the applications are discussed here. One is the porous silicon as an energetic material based on its explosive behavior. The other two are based on the thin film of Si NCs, which are formed in high vacuum: replacing the conventional SiO_2 layer in floating gate in memory devices; as a novel thermoelectric material to convert heat to electricity. Applications in life sciences are also mentioned.

1.16.6.1 Energetic Material

Silicon-based explosive behavior was described for the first time in 1992, when it was reported [113] that potassium nitrate or nitric acid could create explosive-like reactions when reacting with porous silicon. Researchers were investigating the chemiluminescence of anodized silicon, when the addition of concentrated nitric acid to freshly etched porous silicon reacted violently and produced a 'flash of

light with an audible pop'. In 2001, Kovalev *et al.* [114] discovered that hydrogenated porous silicon reacts explosively with condensed or liquid oxygen in the temperature range 4.2–90 K, releasing several times as much energy as an equivalent amount of trinitrotoluene (TNT), at a much greater speed in a timescale of 10^{-6}s. Explosion occurs because the oxygen, which is in a liquid state at the necessary temperatures, is able to oxidize through the porous molecular structure of the silicon extremely rapidly, causing a very quick and efficient detonation. The final products of the reaction are SiO_2 and H_2O, both are nontoxic products. Although hydrogenated porous silicon would probably not be effective as a weapon, due to its functioning only at low temperatures, other uses are being explored for its explosive properties, such as providing thrust for satellites.

A major breakthrough was reported in 2002 after the accidental discovery of a nanoexplosion in porous silicon filled with an oxidant at room temperature [115]. This discovery stimulated the integration of solid-state explosive devices onto silicon chips [116], proving that the explosive porous silicon can be efficiently exploded in negligible amounts.

Kovalev *et al.* [114] proposed the three-step mechanism sketched in **Figure 20**. The match for the explosion is the energy released under the interaction of oxygen molecules with unsaturated (dangling) Si bonds acting as free radicals. Their concentration determined from spin-density measurements [117] in H-terminated porous Si layers is about $10^{16}\,cm^{-3}$ (schematically shown in **Figure 20(a)**). Indeed, the spontaneous reaction has a significantly smaller probability in naturally oxidized samples having the same

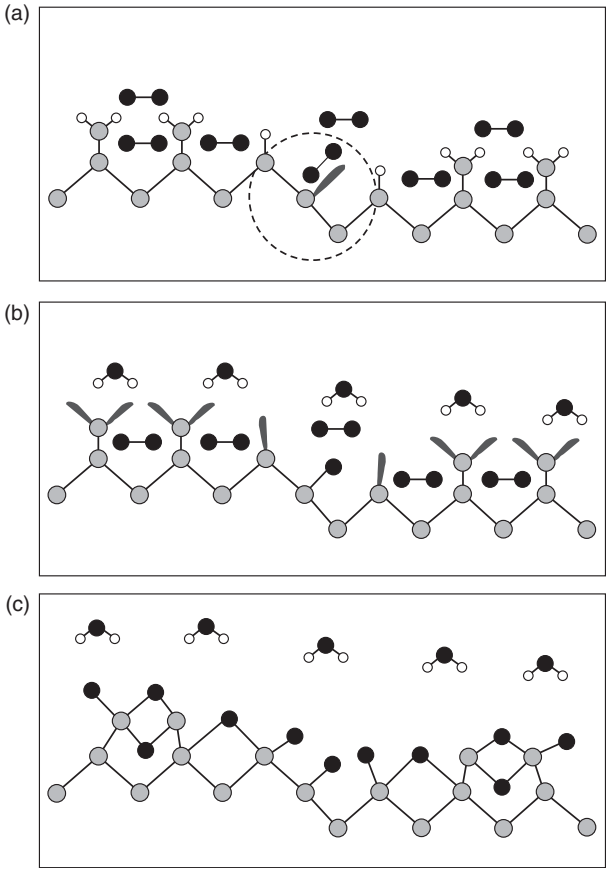

Figure 20 Two-dimensional sketch of the three principal steps (a–c) of the explosive reaction of oxygen with hydrogenated porous silicon. Black circles: oxygen atoms; gray circles: silicon atoms; open circles: hydrogen atoms. The Si dandling bonds are indicated by black lobes. The dashed circumference indicates the ignition site of the reaction. From: Kovalev D, Timoshenko VY, Kunzner N, Gross E, and Koch F (2001) Strong explosive interaction of hydrogenated porous silicon with oxygen at cryogenic temperatures. *Physics Review Letters* 87: 068301.

number of surface Si–H bonds but a smaller number of Si dangling bonds.

Furthermore, while immersions of hydrogen-terminated porous Si layers in liquid oxygen are always accompanied by a spontaneous explosion, for naturally oxidized ones a metastable equilibrium can be realized. In the latter scenario, the explosion can be ignited by pulsed illumination with UV light. UV illumination leads to the rupture of surface Si–H bonds [118] and, therefore, to the creation of dangling bonds igniting the explosive reaction. Another means of ignition is a weak impact. The transformation of the mechanical energy of the impact into the energy for rupturing Si–Si bonds has to be very efficient in porous Si layers since they are a mechanically noncontinuous medium. In a conglomerate of interconnected Si nanometer-sized wires [119], the deformation energy can be concentrated in a certain place and can be high enough to disrupt Si bonds and to form free radicals. Hydrogen atoms covering the internal surface of the porous Si layers play the role of a buffer between Si atoms and molecular oxygen, thus preventing the oxidation reaction. To proceed with the fast oxidation of the internal Si surface further, hydrogen atoms have to be removed by energy transfer to neighboring Si–Hx sites. Indeed, the Si–O bond enthalpy is smaller than that of O–O and a few neighboring dangling bonds are required to ignite the reaction. The Si–Si bonds are weaker than Si–H bonds and in the early stage the breaking of neighboring Si–Si bonds is favorable. However, the oxidation of the Si NC network should be limited by the slow diffusion of oxygen through SiO_2. An almost instantaneous character of the reaction indicates that hydrogen in the second stage of the reaction is removed from the surface. This is favored by an efficient energy transfer between neighboring surface atoms due to their weaker vibronic coupling with the NC core. This is accompanied by the exothermic reaction of oxygen and hydrogen forming water or OH radicals (**Figure 20(b)**). The removal of hydrogen atoms from the surface or the disruption of Si–Si bonds is followed by the formation of new radicals, thus initiating the next step of the reaction: Surface Si atoms interact directly with oxygen, and the oxidation of Si NCs is achieved (**Figure 20(c)**). Interaction of molecular oxygen with dangling bonds also results in the creation of new free radicals in the system, namely, atomic oxygen. Thus, the conditions for a branched chain reaction are fulfilled since all reaction steps create new interacting free radicals: Si dangling bonds, atomic hydrogen and oxygen, or OH groups.

1.16.6.2 Floating Gate in Memory Devices

Many of the potential uses of nanoparticles, for example, as catalysts or magnetic memories, demand that the particles have well-defined sizes. However, this is not easy to accomplish at such small scales, and previously it has been largely a matter of trial and error of size selection. The sublimation of intact alkyl-Si NCs is an extremely novel observation. This method has been used to deposit Si NCs on a variety of substrates placed in the vapor of alkyl-Si NCs (sapphire plates, graphite sheet, silicon wafer, and gold nitride films). Photoemission spectroscopy showed that the alkyl-Si NCs evaporate with no gross chemical changes, but AFM, HRTEM, STM, and confocal luminescence/Raman spectroscopy indicated that the smaller particles are evaporated preferentially. Initially, the NC vapor condensed on the substrate in the form of islands consisting of a single layer of alkyl-Si NCs of height 4.9 ± 0.40 nm. As deposition continued, more islands (2D) were formed, but it was also observed that growth of clusters (3D) of NCs up to 3 μm in diameter. Higher-resolution images were obtained by STM on alkylated *n*-Si (111) substrates in which individual Si NCs could be resolved within the islands. If the source temperature was set to 200°C, the mean diameter of the Si cores was 1.8 ± 0.34 nm for the evaporated material compared to 2.2 ± 0.38 nm for as-prepared alkyl-Si NCs[12,64,71]. The ability to evaporate and deposit NCs in ultrahigh vacuum (UHV) should be useful for the size-controlled preparation of new nanoscale quantum-confined structures. The proposed mechanism for this novel evaporation is a combination of (1) the particle–particle interactions being relatively weak dispersion interactions (various alkyl monolayers on Si have been employed for their antistiction properties) and (2) the thermal stability of the alkyl monolayer on Si being substantially higher (340°C in UHV) than for noncovalently anchored monolayers such as the alkanethiol SAMs, which desorb at about 175°C [120].

The size-controlled NCs thin film could be used to replace the SiO_2 layer in floating-gate memory devices. The ideal memory devices should have such characteristics as high memory performance with fast program/erase cycle speed, low operating power with high drive current, long memory retention time, high reliability, and long lifetime. In current floating-gate memories, charge is stored on a silicon floating gate that is separated from the substrate by a dielectric tunneling barrier.

Si-QD memories, in which the SiO_2 layer is replaced by a Si NCs monolayer, have attracted considerable attention in the last few years [121, 122] as one of the simplest evolutions of the standard flash technology allowing for improved reliability and scaling perspectives.

Currently, nonvolatile memory devices utilize floating-gate field-effect transistor technology to store information, and have many applications, for example, mobile phones, digital cameras, camcorders, MP3 players, digital games, iPods, flash cards, and removable storage devices, which is in a rapidly growing market ($40 billion in 2007 up 12.9% from 2006) [123]. In such floating-gate memories, charge is stored on a silicon floating gate that is separated from the substrate by a dielectric tunneling barrier as shown in **Figure 21**. Typically, the tunneling barrier consists of a thin thermally grown SiO_2 layer. This tunneling barrier controls the retention time and the program/erase speed of the device. When a program bias is applied to the device, charge tunnels through the barrier and remains stored on the floating gate after the program voltage is removed.

Since the tunneling barrier must be able to inject a current during programming and to retain charge, a compromise must be made when designing memory devices that integrate a tunneling barrier. When the barrier is made relatively thick, long charge retention times are achieved, but a higher voltage (and a longer time) is required to program and erase the floating gate. When the barrier is thin, the program and erase process will be more rapid, but charge leakage will reduce the retention time. If a monolayer comprised of Si NC (aka QDs) were to replace the SiO_2 layer, an effective lowering of the barrier would be observed. This barrier-lowering effect allows an increase in the tunnel current density and a subsequent increase in the floating-gate program/erase speed. Furthermore, for a normal flash memory, a major problem is caused by the nonuniformity of the oxide. If there is a weak spot where the leakage current density is larger, it acts as a sink and all stored charge in the floating gate would leak away through it. This problem increases with the thinning of the oxide layer. If the floating gate is replaced with nanoparticles the weak spot only affects a small number of nanoparticles and has no effect on the charge stored in other particles. Therefore, in this design, the thickness of both tunneling barrier oxide and interlevel oxide can be reduced without sacrificing the memory retention time. In flash memory, nanoparticles are embedded in a metal-oxide semiconductor field-effect transistor (MOSFET) as floating gates to store electric charge. Since the shift in the device's threshold depends on the particle size, a wide size distribution would wash out the operating threshold. Thus, size selection is a big issue for this application. However, none of the current research is using this novel evaporation–deposition method [71] to select nanoparticle sizes.

1.16.6.3 A Novel Thermoelectric Material

Currently, the energy shortage and climate changes are the serious problems threatening this planet. In this world, approximately 90% of the power is generated by heat engines that use fossil-fuel combustion as a heat source and typically operate at 30–40% efficiency, such that roughly 15 TW of heat is lost to the environment [124]. Thermoelectric materials convert heat into electric current, if they could be made more efficient at that conversion thermoelectric modules could potentially convert part of this low-grade waste heat to electricity, or as an alternative to photovoltaic cells for converting solar warmth into electricity. Unfortunately, current thermoelectric materials are very expensive to make and are nowhere near efficient enough to be used

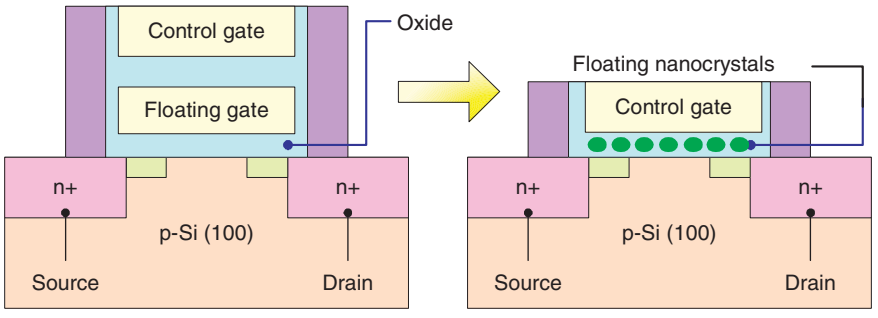

Figure 21 Schematic representation of a floating-gate memory.

commercially. High-performance thermoelectric materials must have large Seebeck coefficient, high electrical conductivity, and low thermal conductivity to retain the heat at the junction and to reduce the heat-transfer losses. The efficiency and energy density of a material for thermoelectric applications is determined by the dimensionless figure of merit

$$ZT = \frac{S^2 \sigma T}{K} = \frac{S^2 \sigma T}{K_L + K_e} \tag{16}$$

where T is the absolute temperature, S is the Seebeck coefficient, σ is the electrical conductivity, and K is the thermal conductivity (K_e is the electronic contribution to the thermal conductivity, K_L is the lattice thermal conductivity). The last decade has seen an enormous research in reducing the thermal conductivity due to phonons in nanostructured materials to enhance the ZT [125]. Silicon, the basic material of semiconductor electronics, is readily available, cheap, and has a huge infrastructure and know-how for its production and manipulation. Those are reasons enough to seek a marriage between silicon and thermoelectric properties [126]. Bulk silicon has a ZT of about 0.01 at 300 K (27°C). For metal wires, the best value at 300 K is about 0.03. Values of 0.7–1.0 are now found in commercially available thermoelectric materials based on bismuth–telluride semiconductors. The first really solid report of much higher figures of merit, up to 2.4, came in 2001, in thin films of a complex semiconductor [127]. But high electrical and thermal losses in these films have so far kept them from the commercial big time. Since $\sigma = \mu pq$ and with Wiedemann–Franz law $K_e/\sigma = L_0 T$ we can rewrite formula 16 as below:

$$ZT = \frac{S^2 \sigma T}{K} = \frac{S^2 \sigma T}{K_L + K_e} = \frac{S^2 T}{\left(\frac{K_L}{\mu pq}\right) + L_0 T} \tag{17}$$

where μ is the carrier mobility for given carrier density p and q is the electronic charge [127]. L_0 is the Lorenz number defined as

$$L_0 = \frac{K_e}{\sigma T}$$

For free electrons in metal

$$L_0 = \frac{K_e}{\sigma T} = \frac{\pi^2}{3}\left(\frac{k_B}{e}\right)^2 = 2.44 \times 10^{-8} \mathrm{w\Omega K^{-2}}$$

When crystalline solids are confined to the nanometer range, phonon transport within them can be significantly altered due to various effects, namely (1) increased boundary scattering; (2) changes in phonon dispersion relation; and (3) quantization of phonon transport. For example, theoretical studies [128,129] have suggested that, as the diameter of a Si nanowire becomes smaller than 20 nm, the phonon dispersion relation could be modified due to phonon confinement, such that the phonon group velocities would be significantly less than the bulk value. Molecular dynamics simulations [130] have shown that, for wires of nanometer diameter, the thermal conductivities could be 2 orders of magnitude smaller than that of bulk silicon [131].

Two independent teams from California have worked out a way to boost the thermoelectric efficiency of silicon by as much as a factor of 100 [124, 132]. Boukai *et al.* [132] used silicon nanowires with a rectangular cross section and Hochbaum *et al.* [124] used round silicon nanowires to achieve thermoelectric efficiencies comparable to those that are the best commercial thermoelectric materials. They believed that this rise in efficiency occurs because heat-carrying sound waves called 'phonons' have a very difficult time moving along the very narrow nanowires, reducing their ability to conduct heat. One important feature of Berkeley nanowires is that their surfaces are rough, which the researchers believe contributes to their high thermoelectric efficiency, although the physics behind this remains unclear. Intriguingly, their observations suggest that another phenomenon – called 'phonon drag' – also plays a role in boosting the thermoelectric efficiency. Phonon drag occurs when phonons moving through the silicon collide with charge carriers such as electrons and drag them along. However, all these research are based on silicon nanowires, and the low efficiency is still the bottleneck.

Figure 22 shows the design of Si NC thermoelectric module, where the thin film of Si NCs produced by the evaporation–deposition process described above. This structure is envisaged to have high figure of merit.

1.16.6.4 Applications in Life Sciences

Nanoparticles have many applications in life sciences, but there is immense concern relating to their potential toxicological hazard to the environment. To mitigate this concern, Si NCs have been suggested as useful nontoxic, red-emitting fluorescent labels. Semiconductor NCs, also known as QDs, are of immense interest for medical imaging because of their controllable photophysical properties.

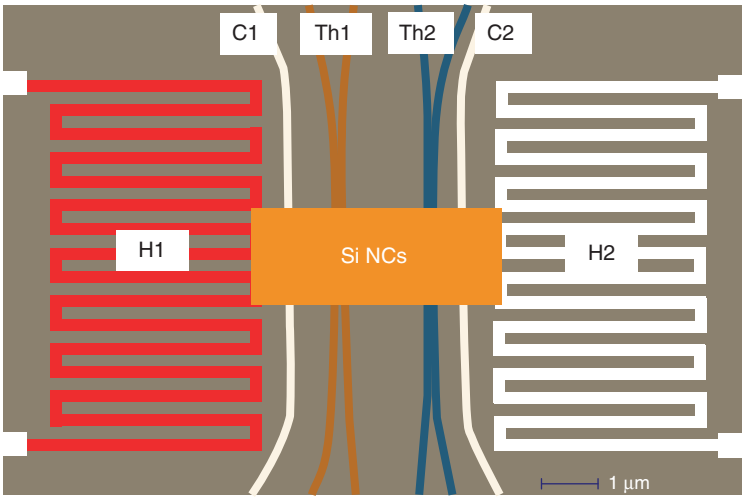

Figure 22 Configuration of silicon nanocrystal thermoelectric module.

NC–antibody conjugates can be designed to target specific cell types and tissues and allow therapeutic agents to be delivered to the affected cells and tissues. It is envisaged that by employing NCs medical diagnostic imaging can be extended beyond merely visualizing gross pathology and cell morphology. NCs are being used to carry out cellular localization of nucleic acids, proteins, and other macromolecules, with the goal of detecting and correcting aberrant disease-related changes in expression. In addition to detecting and localizing molecular defects in gene and protein function, NCs have potential application for correcting cell-specific molecular defects. These applications require a thorough understanding of mechanisms involved in the cellular uptake, and intracellular and subcellular localization of the various types of nanoparticles.

The range and extent of nanoparticle applications is expected to rise, thereby increasing the risk of unwanted exposure to humans as well as the environment. There is, therefore, an urgent need to understand the mechanisms of potentially harmful side effects of these materials, with the view that this understanding will allow the manufacture of NCs with minimal hazardous effects and informed risk assessment. The best understood and most widely used QD fluorophores are based on cadmium chalcogenide NCs. However, *in vitro* studies suggest that under certain conditions this type of nanoparticle may be cytotoxic. This cytotoxicity is primarily attributed to the leaching of heavy metal ions such as Cd^{2+}, but some reports indicate the formation of free radicals. To address this problem alkyl-Si NCs could be the best choice since they are chemically stable and strongly luminescent.

1.16.7 Summary

In this chapter, three types of silicon nanostructures have been discussed: porous silicon, Si NCs, and thin film of Si NCs. After reviewing the synthesis methods, it has been shown how PL spectroscopy reveals the temperature-dependent behavior and origin of two bands in PL emission. Confocal PL spectroscopy enables the characterization of photobleaching and recovery, while near-edge fine band structure and surface states can be demonstrated using XAS and XEOL. Extensive applications of these materials can be expected as energetic materials, and for uses in thermoelectric modules, in electronic devices, and in the life sciences.

References

1. Uhlir A (1956) Electrolytic shaping of germanium and silicon. *Bell Labs Technical Journal* 35(2): 333.
2. Canham LT (1990) Silicon quantum wire array fabrication by electrochemical and chemical dissolution of wafers. *Applied Physics Letters* 57(10): 1046.
3. Heinrich JL, Curtis CL, Credo GM, Kavanagh KL, and Sailor MJ (1992) Luminescent colloidal silicon suspensions from porous silicon. *Science* 255(5040): 66.
4. Kanemitsu Y (1998) Silicon and germanium nanoparticles. In: Lockwood DJ (ed.) *Light Emission in Silicon from Physics to Devices*, p. 164. New York: Academic Press.
5. Lehmann V and Gosele U (1991) Porous silicon formation – A quantum wire effect. *Applied Physics Letters* 58(8): 856.

6. Lie LH, Duerdin M, Tuite EM, Houlton A, and Horrocks BR (2002) Prepararion and characterisation of luminescenct alkylated-silicon quantum dots. *Journal of Electroanalytical Chemistry* 538: 183.
7. Buriak JM (2002) Organometallic chemistry on silicon and germanium surfaces. *Chemical Reviews* 102(5): 1271.
8. Wolkin MV, Jorne J, Fauchet PM, Allan G, and Delerue C (1999) Electronic states and luminescence in porous silicon quantum dots: The role of oxygen. *Physical Review Letters* 82(1): 197.
9. Sweryda-Krawiec B, Cassagneau T, and Fendler JH (1999) Surface modification of silicon nanocrystallites by alcohols. *Journal of Physical Chemistry B* 103(44): 9524.
10. Belomoin G, Therrien J, Smith A, Rao S, Twesten R, Chaieb S, *et al.* (2002) Observation of a magic discrete family of ultrabright Si nanoparticles. *Applied Physics Letters* 80(5): 841.
11. Lie LH, Patole SN, Pike AR, Ryder LC, Connolly BA, Ward AD, *et al.* (2004) Immobilisation and synthesis of DNA on Si(111), nanocrystalline porous silicon and silicon nanoparticles. *Faraday Discussions* 125: 235.
12. Chao Y, Krishnamurthy S, Montalti M, Šiller L, Lie LH, Houlton A, *et al.* (2005) Reactions and luminescence in passivated Si nanocrystallites induced by vacuum ultraviolet and soft-X-ray photons. *Journal of Applied Physics* 98(4): 044316.
13. Baldwin RK, Pettigrew KA, Ratai E, Augustine MP, and Kauzlarich SM (2002) Solution reduction synthesis of surface stabilized silicon nanoparticles. *Chemical Communications* 7(17): 1822.
14. Cichos F, Martin J, and von Borczyskowski C (2004) Emission intermittency in silicon nanocrystals. *Physical Review B* 70(11): 115314.
15. Valenta J, Janda P, Dohnalova K, Niznansky D, Vacha F, and Linnros J (2005) Colloidal suspensions of silicon nanocrystals: From single nanocrystals to photonic structures. *Optical Materials* 27(5): 1046.
16. Lee S, Cho WJ, Chin CS, Han IK, Choi WJ, Park YJ, *et al.* (2004) Optical properties of silicon nanoparticles by ultrasound-induced solution method. *Japanese Journal of Applied Physics* Part 2, 43(6B): L784.
17. Furukawa S and Miyasato T (1988) Quantum size effects on the optical band-gap of microcrystalline Si-H. *Physical Review B* 38(8): 5726.
18. Zhang LB, Coffer JL, and Zerda TW (1998) Properties of luminescent Si nanoparticles in sol-gel matrices. *Journal of Sol-Gel Science and Technology* 11(3): 267.
19. Kovalev D, Heckler H, Ben-Chorin M, Polisski G, Schwartzkopff M, and Koch F (1998) Breakdown of the k-conservation rule in Si nanocrystals. *Physical Review Letters* 81(13): 2803.
20. Choi BH, Hwang SW, Kim IG, Shin HC, Kim Y, and Kim EK (1998) Fabrication and room-temperature characterization of a silicon self-assembled quantum-dot transistor. *Applied Physics Letters* 73(21): 3129.
21. Wilcoxon JP, Samara GA, and Provencio PN (1999) Optical and electronic properties of Si nanoclusters synthesized in inverse micelles. *Physical Review B* 60(4): 2704.
22. Tilley RD, Warner JH, Yamamoto K, Matsui I, and Fujimori H (2005) Micro-emulsion synthesis of monodisperse surface stabilized silicon nanocrystals. *Chemical Communications* (14): 1833.
23. Hata K, Yoshida S, Fujita M, Yasuda S, Makimura T, Murakami K, *et al.* (2001) Self-assembled monolayer as a template to deposit silicon nanoparticles fabricated by laser ablation. *Journal of Physical Chemistry B* 105(44): 10842.
24. Kapaklis V, Politis C, Poulopoulos P, and Schweiss P (2005) Photoluminescence from silicon nanoparticles prepared from bulk amorphous silicon monoxide by the disproportionation reaction. *Applied Physics Letters* 87(12): 123114.
25. Liu SM, Sato S, and Kimura K (2005) Synthesis of luminescent silicon nanopowders redispersible to various solvents. *Langmuir* 21(14): 6324.
26. Schoenfeld O, Zhao X, Christen J, Hempel T, Nomura S, and Aoyagi Y (1996) Formation of Si quantum dots in nanocrystalline silicon. *Solid-State Electronics* 40(1–8): 605.
27. Dinh LN, Chase LL, Balooch M, Siekhaus WJ, and Wooten F (1996) Optical properties of passivated Si nanocrystals and SiO_x nanostructures. *Physical Review B* 54(7): 5029.
28. van Buuren T, Dinh LN, Chase LL, Siekhaus WJ, and Terminello LJ (1998) Changes in the electronic properties of Si nanocrystals as a function of particle size. *Physical Review Letters* 80(17): 3803.
29. English DS, Pell LE, Yu ZH, Barbara PF, and Korgel BA (2002) Size tunable visible luminescence from individual organic monolayer stabilized silicon nanocrystal quantum dots. *Nano Letters* 2(7): 681.
30. Fojtik A and Henglein A (1994) Luminescent colloidal silicon particles. *Chemical Physics Letters* 221(5–6): 363.
31. Holmes JD, Ziegler KJ, Doty RC, Pell LE, Johnston KP, and Korgel BA (2001) Highly luminescent silicon nanocrystals with discrete optical transitions. *Journal of the American Chemical Society* 123(16): 3743.
32. Li XG, He YQ, Talukdar SS, and Swihart MT (2003) Process for preparing macroscopic quantities of brightly photoluminescent silicon nanoparticles with emission spanning the visible spectrum. *Langmuir* 19(20): 8490.
33. Littau KA, Szajowski PJ, Muller AJ, Kortan AR, and Brus LE (1993) A luminescent silicon nanocrystal colloid via a high-temperature aerosol reaction. *Journal of Physical Chemistry* 97(6): 1224.
34. Bley RA and Kauzlarich SM (1996) A low-temperature solution phase route for the synthesis of silicon nanoclusters. *Journal of the American Chemical Society* 118(49): 12461.
35. Liu Q and Kauzlarich SM (2002) A new synthetic route for the synthesis of hydrogen terminated silicon nanoparticles. *Materials Science and Engineering B* 96(2): 72.
36. Zou J, Baldwin RK, Pettigrew KA, and Kauzlarich SM (2004) Solution synthesis of ultrastable luminescent siloxane-coated silicon nanoparticles. *Nano Letters* 4(7): 1181.
37. Botti S, Terranova ML, Sessa V, Piccirillo S, and Rossi M (2001) Silicon quantum dots in diamond matrix: A new synthesis route. *Applied Organometallic Chemistry* 15(5): 388.
38. Giesen B, Wiggers H, Kowalik A, and Roth P (2005) Formation of Si-nanoparticles in a microwave reactor: Comparison between experiments and modelling. *Journal of Nanoparticle Research* 7(1): 29.
39. Mangolini L, Thimsen E, and Kortshagen U (2005) High-yield plasma synthesis of luminescent silicon nanocrystals. *Nano Letters* 5(4): 655.
40. Sankaran RM, Holunga D, Flagan RC, and Giapis KP (2005) Synthesis of blue luminescent Si nanoparticles using atmospheric-pressure microdischarges. *Nano Letters* 5(3): 537.
41. Valenta J, Juhasz R, and Linnros J (2002) Photoluminescence spectroscopy of single silicon quantum dots. *Applied Physics Letters* 80(6): 1070.

42. Van Buuren T, Tiedje T, Dahn JR, and Way BM (1993) Photoelectron-spectroscopy measurements of the band-gap in porous silicon. *Applied Physics Letters* 63(21): 2911.
43. Fauchet PM (1998) Porous silicon: Photoluminescence and electroluminescent devices. In: Lockwood DJ (ed.) *Light Emission in Silicon from Physics to Devices*, p. 205. New York: Academic Press.
44. Kapoor M, Singh VA, and Johri GK (2000) Origin of the anomalous temperature dependence of luminescence in semiconductor nanocrystallites. *Physical Review B* 61(3): 1941.
45. Kanemitsu Y (1996) Photoluminescence spectrum and dynamics in oxidized silicon nanocrystals: A nanoscopic disorder system. *Physical Review B* 53(20): 13515.
46. Suemoto T, Tanaka K, and Nakajima A (1994) Interpretation of the temperature-dependence of the luminescence intensity, lifetime, and decay profiles in porous Si. *Physical Review B* 49(16): 11005.
47. Komuro S, Kato T, Morikawa T, Okeeffe P, and Aoyagi Y (1996) Carrier dynamics in oxidized porous silicon. *Journal of Applied Physics* 80(3): 1749.
48. Gaponenko SV, Petrov EP, Woggon U, Wind O, Klingshirn C, Xie YH, *et al.* (1996) Steady-state and time-resolved spectroscopy of porous silicon. *Journal of Luminescence* 70: 364.
49. Dixon DA and Gole JL (2005) Time-dependent density functional theory predictions of the vertical excitation energies of silanones as models for the excitation process in porous silicon. *Journal of Physical Chemistry B* 109(31): 14830.
50. ElShall MS, Li S, Turkki T, Graiver D, Pernisz UC, and Baraton MI (1995) Synthesis and photoluminescence of weblike agglomeration of silica nanoparticles. *Journal of Physical Chemistry* 99(51): 17805.
51. Germanenko IN, Dongol M, Pithawalla YB, El-Shall MS, and Carlisle JA (1999) Effect of atmospheric oxidation on the electronic and photoluminescence properties of silicon nanocrystals. In: *1st IUPAC Workshop on Advanced Material (WAM1).* Hong Kong, Peoples Republic of China.
52. Zhang Q, Bayliss SC, Alajili A, Hutt DA, and Harris P (1994) The blue photoluminescence and nanostructure of Si-clusters and C-clusters embedded in SiO_2 matrices. In: *1st European Conference on Synchrotron Radiation in Materials Science.* Chester, England.
53. Liu WL, Zhang M, Lin CL, Zeng ZM, Wang LW, and Chu PK (2001) Intense blue-light emission from carbon-plasma-implanted porous silicon. *Applied Physics Letters* 78(1): 37.
54. Itoh C, Tanimura K, Itoh N, and Itoh M (1989) Threshold energy for photogeneration of self-trapped excitons in SiO_2. *Physical Review B* 39(15): 11183.
55. Sham TK, Naftel SJ, Kim PSG, Sammynaiken R, Tang YH, Coulthard I, *et al.* (2004) Electronic structure and optical properties of silicon nanowires: A study using X-ray excited optical luminescence and X-ray emission spectroscopy. *Physical Review B* 70(4): 045313.
56. Reboredo FA and Galli G (2005) Theory of alkyl-terminated silicon quantum dots. *Journal of Physical Chemistry B* 109(3): 1072.
57. Osad'ko IS (2005) Model for power-law statistics in blinking photoluminescence of single semiconductor nanocrystals. *Chemical Physics* 316(1–3): 99.
58. Tang J and Marcus RA (2005) Mechanisms of fluorescence blinking in semiconductor nanocrystal quantum dots. *Journal of Chemical Physics* 123(5): 054704.
59. Verberk R, van Oijen AM, and Orrit M (2002) Simple model for the power-law blinking of single semiconductor nanocrystals. *Physical Review B* 66(23): 233202.
60. John GC and Singh VA (1996) Model for the photoluminescence behavior of porous silicon. *Physical Review B* 54(7): 4416.
61. Banerjee S (1994) Light-emission from porous silicon. *Bell Labs Technical Journal* 17(5): 533.
62. Kanemitsu Y, Uto H, Masumoto Y, Matsumoto T, Futagi T, and Mimura H (1993) Microstructure and optical-properties of freestanding porous silicon films – size dependence of absorption-spectra in Si nanometer-sized crystallites. *Physical Review B* 48(4): 2827.
63. Cullis AG, Canham LT, and Calcott PDJ (1997) The structural and luminescence properties of porous silicon. *Journal of Applied Physics* 82(3): 909.
64. Chao Y, Houlton A, Horrocks BR, Hunt MRC, Poolton NRJ, Yang J, *et al.* (2006) Optical luminescence from alkyl-passivated Si nanocrystals under vacuum ultraviolet excitation: Origin and temperature dependence of the blue and orange emissions. *Applied Physics Letters* 88(26): 263119.
65. Efros AL and Rosen M (1997) Random telegraph signal in the photoluminescence intensity of a single quantum dot. *Physical Review Letters* 78(6): 1110.
66. Credo GM, Mason MD, and Buratto SK (1999) External quantum efficiency of single porous silicon nanoparticles. *Applied Physics Letters* 74(14): 1978.
67. Rostron RJ, Chao Y, Roberts G, and Horrocks BR (2009) Simultaneous photocharging and luminescence intermittency in silicon nanocrystals. *Journal of Physics: Condensed Matter* 21(23): 8.
68. Macdonald JR (1963) Transient and temperature response of a distributed, thermally activated system. *Journal of Applied Physics* 34(3): 538.
69. Macdonald JR (1987) Linear relaxation – distributions, thermal-activation, structure, and ambiguity. *Journal of Applied Physics* 62(11): R51.
70. Albery WJ, Bartlett PN, Wilde CP, and Darwent JR (1985) A general-model for dispersed kinetics in heterogeneous systems. *Journal of the American Chemical Society* 107(7): 1854.
71. Chao Y, Šiller L, Krishnamurthy S, Coxon PR, Bangert U, Gass M, *et al.* (2007) Evaporation and deposition of alkyl-capped silicon nanocrystals in ultrahigh vacuum. *Nature Nanotechnology* 2(8): 486.
72. Chen JG (1997) NEXAFS investigations of transition metal oxides, nitrides, carbides, sulfides and other interstitial compounds. *Surface Science Reports* 30(1–3): 1.
73. Stohr J (1992) *NEXAFS Spectroscopy: Springer Series in Surface Science*, vol. 25. New York: Springer.
74. Käämbre T (2002) *Resonant Soft X-ray Spectroscopic Studies of C60 and Related Materials.* Doctoral thesis, Comprehensive Summary, Physics. Uppsala: Acta Universitatis Upsaliensis.
75. Gensterblum G, Hevesi K, Han BY, Yu LM, Pireaux JJ, Thiry PA, *et al.* (1994) Growth mode and electronic-structure of the epitaxial C- 60(111)/Ges(001) interface. *Physical Review B* 50(16): 11981.
76. Stevens PA, Upton TH, Stohr J, and Madix RJ (1991) Chemisorption-induced changes in the X-ray-absorption fine-structure of adsorbed species. *Physical Review Letters* 67(12): 1653.
77. Wuhn A, Weckesser J, and Woll C (2001) Bonding and orientational ordering of long-chain carboxylic acids on Cu(111): Investigations using X-ray absorption spectroscopy. *Langmuir* 17(24): 7605.
78. Eisebitt S, Boske T, Rubensson JE, and Eberhardt W (1993) Determination of absorption-coefficients for concentrated samples by fluorescence detection. *Physical Review B* 47(21): 14103.

79. Stohr J, Kollin EB, Fischer DA, Hastings JB, Zaera F, and Sette F (1985) Surface extended X-ray-absorption fine-structure of low-Z adsorbates studied with fluorescence detection. *Physical Review Letters* 55(14): 1468.
80. Hu YF, Boukherroub R, and Sham TK (2004) Near edge X-ray absorption fine structure spectroscopy of chemically modified porous silicon. *Journal of Electron Spectroscopy and Related Phenomena* 135(2–3): 143.
81. Kasrai M, Yin ZF, Bancroft GM, and Tan KH (1993) X-ray-fluorescence measurements of X-ray-absorption near-edge structure at the Si, P, and S L-edges. *Journal of Vacuum Science and Technology A* 11(5): 2694.
82. Gong XG (1995) Stability and electronic properties of nanoscale silicon clusters. *Physical Review B* 52(20): 14677.
83. Katlrcloglu S and Erkoç S (2001) Structural and electronic properties of bare and hydrogenated silicon clusters. *Physica E* 9(2): 314.
84. Bianconi A (1979) Core excitons and inner well resonances in surface soft X-ray absorption (SSXA) spectra. *Surface Science* 89: 41.
85. Tanaka I, Kawai J, and Adachi H (1995) Near-edge X-ray-absorption fine structure of crystalline silicon dioxides. *Physical Review B* 52(16): 11733.
86. Wu ZY, Jollet F, and Seifert F (1998) Electronic structure analysis of alpha-SiO_2 via X-ray absorption near-edge structure at the Si K, L-2,L-3 and O K edges. *Journal of Physics: Condensed Matter* 10(36): 8083.
87. Eisebitt S, Lüning J, Rubensson JE, van Buuren T, Patitsas SN, Tiedje T, *et al.* (1996) Quantum confinement effects in the soft X-ray fluorescence spectra of porous silicon nanostructures. *Solid State Communication* 97(7): 549.
88. Eisebitt S, Lüning J, Rubensson JE, van Buuren T, Patitsas SN, Tiedje T, *et al.* (1996) Soft X-ray emission of porous silicon nanostructures. *Journal of Electron Spectroscopy and Related Phenomena* 79: 135.
89. Brown FC and Rustgi OP (1972) Extreme ultraviolet transmission of crystalline and amorphous silicon. *Physical Review Letters* 28(8): 497.
90. Sychugov I, Juhasz R, Valenta J, and Linnros J (2005) Narrow luminescence linewidth of a silicon quantum dot. *Physical Review Letters* 94(8): 087405.
91. Brown FC, Bachrach RZ, and Skibowski M (1977) L2,3 threshold spectra of doped silicon and silicon compounds. *Physical Review B* 15(10): 4781.
92. Kane EO (1966) Band structure of silicon from an adjusted Heine-Abarenkov calculation. *Physical Review* 146(2): 558.
93. Batson PE and Bruley J (1991) Dynamic screening of the core exciton by swift electrons in electron-energy-loss scattering. *Physical Review Letters* 67(3): 350.
94. Altarelli M and Dexter DL (1972) Core excitons and the soft-X-ray threshold of silicon. *Physical Review Letters* 29(16): 1100.
95. Suda Y, Obata K, and Koshida N (1998) Band dispersions in photoluminescent porous Si. *Physical Review Letters* 80(16): 3559.
96. Lu ZH, Lockwood DJ, and Baribeau JM (1995) Quantum confinement and light-emission in SiO_2/Si Superlattices. *Nature* 378(6554): 258.
97. Zimina A, Eisebitt S, Eberhardt W, Heitmann J, and Zacharias M (2006) Electronic structure and chemical environment of silicon nanoclusters embedded in a silicon dioxide matrix. *Applied Physics Letters* 88(16): 163103.
98. Willey TM, Bostedt C, van Buuren T, Dahl JE, Liu SG, Carlson RMK, *et al.* (2005) Molecular limits to the quantum confinement model in diamond clusters. *Physical Review Letters* 95(11): 113401.
99. Sham TK, Sammynaiken R, Zhu YJ, Zhang P, Coulthard I, and Naftel SJ (2000) X-ray excited optical luminescence (XEOL): A potential tool for OELD studies. *Thin Solid Films* 363(1–2): 318.
100. Bianconi A, Jackson D, and Monahan K (1978) XEOL note. *Physical Review B* 17: 2021.
101. Soderholm L, Liu GK, Antonio MR, and Lytle FW (1998) X-ray excited optical luminescence (XEOL) detection of X-ray absorption fine structure (XAFS). *Journal of Chemical Physics* 109(16): 6745.
102. Sham TK, Jiang DT, Coulthard I, Lorimer JW, Feng XH, Tan KH, *et al.* (1993) Origin of luminescence from porous silicon deduced by synchrotron-light-induced optical luminescence. *Nature* 363(6427): 331.
103. Jiang DT, Coulthard I, Sham TK, Lorimer JW, Frigo SP, Feng XH, *et al.* (1993) Observations on the surface and bulk luminescence of porous silicon. *Journal of Applied Physics* 74(10): 6335.
104. Coulthard I and Sham TK (1999) Luminescence from porous silicon: an optical X-ray absorption fine structures study at the Si L3,2-edge. *Solid State Communications* 110(4): 203.
105. Kanemitsu Y, (2002) Efficient light emission from crystalline and amorphous silicon nanostructures. *Journal of Luminescence* 100: 209.
106. Kanemitsu Y, Fukunishi Y, Iiboshi M, Okamoto S, and Kushida T (2000) Visible luminescence from Si/SiO_2 quantum wells and dots: Confinement and localization of excitons. *Physica E* 7(3–4): 456.
107. Brus LE, Szajowski PF, Wilson WL, Harris TD, Schuppler S, and Citrin PH (1995) Electronic spectroscopy and photophysics of Si nanocrystals: Relationship to bulk c-Si and porous Si. *Journal of the American Chemical Society* 117: 2915.
108. Fauchet PM, Ettedgui E, Raisanen A, Brillson LJ, Seiferth F, Kurinec SK, *et al.* (1993) Can oxidation and other treatments help us understand the nature of light-emitting porous silicon. *Silicon-Based Optoelectronic Materials* 298: 271.
109. Batson PE and Heath JR (1993) Electron-energy-loss spectroscopy of single silicon nanocrystals – the conduction-band. *Physical Review Letters* 71(6): 911.
110. Pettifer RF, Glanfield A, Gardelis S, Hamilton B, Dawson P, and Smith AD (1995) X-ray excited optical luminescence (XEOL) study of porous silicon. *Physica B* 209(1–4): 484.
111. Coulthard I, Antel WJ, Freeland JW, Sham TK, Naftel SJ, and Zhang P (2000) Influence of sample oxidation on the nature of optical luminescence from porous silicon. *Applied Physics Letters* 77(4): 498.
112. Torchynska TV, Rodriguez MM, Polupan GP, Khomenkova LI, Korsunskaya NE, Papusha VP, *et al.* (2001) USXES and optical phenomena in Si low-dimensional structures dependent on morphology and silicon oxide composition on Si surface. In: *13th International Conference on Vacuum Ultraviolet Radiation Physics (VUV-13).* Trieste: World Scientific.
113. McCord P, Yau SL, and Bard AJ (1992) Chemiluminescence of anodized and etched silicon – evidence for a luminescent siloxene-like layer on porous silicon. *Science* 257(5066): 68.
114. Kovalev D, Timoshenko VY, Kunzner N, Gross E, and Koch F (2001). Strong explosive interaction of hydrogenated porous silicon with oxygen at cryogenic temperatures. *Physical Review Letters* 87(6): 068301.
115. Mikulec FV, Kirtland JD, and Sailor MJ (2002) Explosive nanocrystalline porous silicon and its use in atomic emission spectroscopy. *Advanced Materials* 14(1): 38.

116. du Plessis M (2007) Properties of porous silicon nano-explosive devices. *Sensors and Actuators A* 135(2): 666.
117. Meyer BK, Petrovakoch V, Muschik T, Linke H, Omling P, and Lehmann V (1993) Electron-spin-resonance investigations of oxidized porous silicon. *Applied Physics Letters* 63(14): 1930.
118. Timoshenko VY, Dittrich T, Koch F, Kamenev BV, and Rappich J (2000) Annihilation of nonradiative defects on hydrogenated silicon surfaces under pulsed-laser irradiation. *Applied Physics Letters* 77(19): 3006.
119. Cullis AG and Canham LT (1991) Visible-light emission due to quantum size effects in highly porous crystalline silicon. *Nature* 353(6342): 335.
120. Faucheux A, Yang F, Allongue P, De Villeneuve CH, Ozanam F, and Chazalviel JN (2006) Thermal decomposition of alkyl monolayers covalently grafted on (111) silicon. *Applied Physics Letters* 88(19): 3.
121. Feng T, Yu HB, Dicken M, Heath JR, and Atwater HA (2005) Probing the size and density of silicon nanocrystals in nanocrystal memory device applications. *Applied Physics Letters* 86(3): 033103.
122. Rao RA, Gasquet HP, Steimle RF, Rinkenberger G, Straub S, Muralidhar R, *et al.* (2005) Influence of silicon nanocrystal size and density on the performance of non-volatile memory arrays. *Solid-State Electron* 49(11): 1722.
123. http://www.isuppli.com – iSuppli.
124. Hochbaum AI, Chen RK, Delgado RD, Liang WJ, Garnett EC, Najarian M, *et al.* (2008) Enhanced thermoelectric performance of rough silicon nanowires. *Nature* 451: 163.
125. Prasher R (2006) Thermal conductivity of composites of aligned nanoscale and microscale wires and pores. *Journal of Applied Physics* 100: 034307.
126. Vining CB (2008) Desperately seeking silicon. *Nature* 451: 255.
127. Venkatasubramanian R, Siivola E, Colpitts T, and O'Quinn B (2001) Thin-film thermoelectric devices with high room-temperature figures of merit. *Nature* 413(6856): 597.
128. Balandin A and Wang KL (1998) Significant decrease of the lattice thermal conductivity due to phonon confinement in a free-standing semiconductor quantum well. *Physical Review B* 58(3): 1544.
129. Khitun A, Balandin A, and Wang KL (1999) Modification of the lattice thermal conductivity in silicon quantum wires due to spatial confinement of acoustic phonons. *Superlattices and Microstructures* 26(3): 181.
130. Volz SG and Chen G (1999) Molecular dynamics simulation of thermal conductivity of silicon nanowires. *Applied Physics Letters* 75(14): 2056.
131. Li D, Wu Y, Fan R, Yang P, and Majumdar A (2003) Thermal conductivity of Si/SiGe superlattice nanowires. *Applied Physics Letters* 83(15): 3186.
132. Boukai AI, Bunimovich Y, Tahir-Kheli J, Yu JK, Goddard WA, and Heath JR (2008) Silicon nanowires as efficient thermoelectric materials. *Nature* 451: 168.